Accepted Manuscript

Geochemistry: Exploration, Environment, Analysis

Assessing copper fertility of intrusive rocks using field portable X-Ray fluorescence (pXRF) data

Ayesha Ahmed, Anthony J. Crawford, Christopher Leslie, Joshua Phillips, Tristan Wells, Amos Garay, Shawn B. Hood & David R. Cooke

DOI: https://doi.org/10.1144/geochem2018-077

Received 16 November 2018
Revised 23 March 2019
Accepted 25 March 2019

Supplementary material at https://doi.org/10.6084/m9.figshare.c.4447769

To cite this article, please follow the guidance at http://www.geolsoc.org.uk/onlinefirst#cit_journal

Assessing copper fertility of intrusive rocks using field portable X-Ray fluorescence (pXRF) data

Ayesha Ahmed*[1], Anthony J. Crawford[2], Christopher Leslie[2], Joshua Phillips[1], Tristan Wells[2], Amos Garay[1], Shawn B. Hood[1] and David R. Cooke[1]

[1] Transforming the Mining Value Chain, An ARC Industrial Transformation Research Hub, CODES, University of Tasmania, Hobart, Tasmania, Australia

[2] Centre for Ore Deposit and Earth Sciences (CODES), University of Tasmania, Hobart, Tasmania, Australia

***Corresponding author (email: Ayesha.Ahmed@utas.edu.au)**

Abbreviated Title: Porphyry copper prospectivity using pXRF

Abstract

Based on a global compilation of whole-rock geochemical data, Sr/Y and Sr/MnO are identified as effective discriminators between ore-forming and unprospective intrusions in the porphyry Cu setting. Intrusive rocks are classified into three fertility groups: prospective, unprospective, and mixed-signal, which are designed to assist explorers as a discrimination tool, narrowing the exploration search-space in porphyry Cu districts.

Portable X-Ray fluorescence (pXRF) data of Sr, Y and MnO were collected on pulp powders and rock slabs from six porphyry Cu (± Mo ± Au) districts. Pre- and post-mineralization intrusions from porphyry Cu districts have lower Sr/Y and Sr/MnO values than syn-mineralization intrusions from the same districts, although absolute values were variable between districts.

PXRF data were compared to conventional whole-rock data to determine if pXRF data were appropriate substitutes for conventional whole-rock methods of evaluating the ore-forming potential of intrusive rocks. PXRF data collected on pulp material were found to be more accurate (<16% of conventional methods) and more precise (<5% relative standard deviation) than those collected on intact rock slabs (<37% of conventional methods; <24% relative standard deviation). These differences are attributed to the grain size and mineral homogeneity of samples. Despite the low precision of pXRF analyses on individual rock slabs (mean RSD of 24% Sr/Y and 32% Sr/MnO), mean values for each sample plot in the expected fertility field on the Sr/Y and Sr/MnO diagram. Our results demonstrate that *in*

situ pXRF data collection provides an effective discriminator of Cu fertility, and represents a powerful field exploration tool.

END OF ABSTRACT

****

The ore-forming potential of intrusive rocks in the porphyry Cu environment can be assessed using bulk-rock compositions, particularly variations in SiO_2, Sr, Y, Mn, La and Yb contents (e.g., Baldwin and Pearce, 1982; Richards and Kerrich, 2007; Loucks, 2014). Magmas associated with porphyry Cu mineralization are typically oxidised and hydrous (Ballard et al., 2002; Mungall, 2002; Cooke et al., 2005; Sillitoe, 2010, Sun et al., 2013) and are associated with arc rocks that have characteristically high La/Yb_n and Sr/Y values, and low Mn contents (Baldwin and Pearce, 1982; Thiéblemont et al., 1997; Richards and Kerrich, 2007; Richards, 2012; Loucks, 2014). Amphibole can accommodate significant amounts of Mn and Y into its structure (Greenland et al., 1968; Sisson, 1994). High magmatic water contents (≥4 wt.%) promote amphibole formation and early amphibole fractionation (or garnet fractionation during high pressure fractionation), resulting in progressively lower Mn and Y-contents as hydrous magmas evolve (Baldwin and Pearce, 1982; Richards and Kerrich, 2007). Under the same hydrous conditions, plagioclase crystallisation is supressed, resulting in evolved magmas with high Sr-contents (Richards and Kerrich, 2007). Under oxidised conditions, titanite and/or magnetite are stable (Richards, 2003; Costa et al., 2004; Castillo, 2012; Loader at al., 2017). Progressive fractionation of hornblende and titanite ± magnetite ± garnet increases the La/Yb_n and Sr/Y ratios of magmas (Sisson, 1994; Castillo et al., 1999; Bachman et al., 2005; Rooney et al., 2010; Loucks, 2014).

Copper prospectivity diagrams can illustrate the potential of intrusive rock suites to form porphyry and high-sulfidation ore deposits (Baldwin and Pearce, 1982; Ballard et al., 2002; Richards and Kerrich, 2007; Loucks, 2014). These diagrams use rock samples from known areas of mineralization to produce thresholds that correspond to prospective or unprospective compositions. Global compilations of whole-rock geochemical data independently show that relative to unmineralized magmatic rocks, ore-forming intrusions in subduction-related tectonic environments are characterised by elevated Sr, low Y, and low MnO (Baldwin and Pearce, 1982; Richards and Kerrich, 2007; Loucks, 2014). Existing studies using data for these elements have proposed fertility discrimination diagrams using:

Sr/Y vs. Y; Sr/Y vs. SiO_2, and Y vs. MnO (Baldwin and Pearce, 1982; Loucks, 2014). In this study, we combine the indices from several studies into a single bivariate plot of Sr/Y vs. Sr/MnO.

Traditional Cu prospectivity diagrams use geochemical data collected by conventional methods such as ICP-MS, ICP-ES or XRF (e.g., Baldwin and Pearce, 1982; Richards and Kerrich, 2007; Loucks, 2014). The cost and time of conventional laboratory analyses may limit the number of samples analysed. These conventional whole-rock datasets are typically interpreted after field exploration has been conducted and analytical results have been returned from the laboratory. As such, the results do not necessarily provide real-time insight or inform decision making during field sampling or drilling programmes.

In this paper, we show that: (1) based on a global compilation of data, whole-rock values of Sr/Y and Sr/MnO can effectively discriminate between ore-forming and unprospective intrusions in the porphyry Cu environment; and (2) pXRF data, calibrated to ICP-MS/ICP-ES data, can be used in place of conventional whole-rock analytical data to inform the Sr/Y vs Sr/MnO Cu prospectivity discrimination diagram. We present comparisons of conventional ICP-MS/ICP-ES and pXRF results from six mineralized districts: (1) the Yerington porphyry Cu (±Mo-Au) district, USA; (2) the Resolution porphyry Cu-Mo deposit, USA; (3) the Las Bambas Cu-Fe skarn district, Peru; (4) the Cadia Cu-Au district, Australia; (5) the Northparkes Cu-Au district, Australia; and (6) the Cowal Cu-Au district, Australia. To demonstrate that pXRF data can be acquired directly from unprocessed rocks in the field, we evaluate the accuracy and precision of pXRF data collected from both pulp material (120 mesh) and intact rock slabs (up to 0.5 cm grain size), to conventional ICP-MS/ICP-ES whole-rock data.

Geology of pXRF sample locations

Figure 1 shows the geographic location of each ore deposit district from which samples were analysed using pXRF. The deposit-type and igneous geochronology of samples used in this study are described in Table 1. Where absolute (radiometric) ages of intrusions are unavailable, the relative age of each intrusion (pre-, syn-, or post-mineralization) was determined based on cross-cutting relationships identified by field-mapping or in drill core.

Yerington district, USA

The Yerington mining district (Yerington) in western Nevada, USA (Fig. 1) is a well-mapped, well-studied area that contains porphyry Cu and skarn deposits (Fig. 1; Einaudi, 1977; Harris and Einaudi, 1982; Proffett and Dilles, 1984; Dilles, 1987; Dilles and Einaudi, 1992). The combined geological resource and production of the district is in excess of 6 Mt Cu in sulfide ores and >100 Mt of Fe in oxide ores (Dilles and Proffett, 1995). The Ann Mason deposit, in the Yerington district, has a combined measured and indicated mineral resource of 4.49 Mt Cu, 84.8 kt Mo, and 37.7 t Au (Kulla et al., 2015). Ann Mason, and other porphyry and skarn Cu deposits in the district (e.g., Casting Copper, and Ludwig), are associated with the Luhr Hill granite and granite porphyry dykes, part of the Yerington batholith (Proffett and Dilles, 1984; Dilles, 1987; Dilles and Wright, 1988). The Yerington batholith is a medium- to high-K calc-alkaline polyphase intrusive complex (Dilles, 1987). The batholith intruded a sequence of sedimentary and volcanic rocks over a span of 1 m.y. (Dilles and Wright, 1988). Intrusive phases include the pre-mineralization McLeod Hill quartz monzodiorite (169.4 ± 0.4 Ma; Dilles and Wright, 1988) and Bear quartz monzonite; syn-mineralization units include the Luhr Hill granite and associated granite porphyry dykes (168.5 ± 0.4 Ma; Dilles and Wright, 1988). The Shamrock monzonite post-dates Cu-mineralization in the district (165.8 ± 0.4 Ma; Dilles and Wright, 1988).

Resolution, USA

The Resolution porphyry Cu deposit is in the Superior district, which occurs along a prominent east-northeast trending, 50 km long belt of porphyry Cu deposits in, Arizona, USA (Fig. 1; Ballantyne et al., 2003). In 2012, Resolution had an inferred resource of 1,787 Mt at 1.54% Cu and 0.035% Mo (Henke et al., 2012). The deposit is concealed beneath 1.5 km of post-mineralization cover and only minor volumes of felsic intrusive rocks are exposed at surface. The pre-mineralization intrusion, a 2 by 3 km quartz diorite stock intruded Proterozoic and Paleozoic rocks 6 km northwest of Resolution, at the Silver King prospect. The quartz diorite stock is intruded by a smaller porphyritic intrusion of dacitic composition. Throughout the district, the pre-mineral sequence of Proterozoic to Paleozoic rocks has been crosscut by narrow dacitic dykes and sills, which are particularly well-developed in the Magma mine (Hammer and Peterson, 1968) and at Resolution (Manske and Paul, 2002; Henke et al., 2012). Approximately 12 km to the northeast of Resolution is the polyphase

Schultze Granite. The Schultze Granite is composed of up to 15 texturally distinct, but chemically indistinguishable intrusive phases, (Creasy, 1980, 1984; Stavast, 2006). The Schultze granite is widely interpreted as the causative pluton for mineralization in the local Globe-Miami and Superior districts (Creasy, 1980; Stavast, 2006; Maher, 2008).

Las Bambas, Peru

The Las Bambas Cu skarn district in southern Peru is within the Andahuaylas-Yauri belt (Fig. 1) and consists of three deposit centres: Chalcobamba, Ferrobamba, and Sulfabamba. The total Cu resource for the Las Bambas district is 1,873 Mt at 0.85% Cu (2017; www.mmg.com). Copper skarn mineralization is associated with late Eocene quartz-diorite plutons, including the Jahuapaylla monzodiorite, Ferrobamba monzodiorite, and La Cresta monzodiorite (Cannell et al., 2017). Copper skarn ore from the main mineralization event is crosscut by post-mineralization quartz monzodiorite porphyry stocks and swarms of monzogranite and monzodiorite dykes. The Pioneros quartz diorite stock and the Rayusco diorite, to the north of Ferrobamba, are unmineralized and pre-date mineralization at Las Bambas (Cannell et al., 2017).

Cadia, New South Wales, Australia

The Cadia Valley district, central NSW, Australia, is one of the largest and most metal-endowed alkalic porphyry camps in the world (Fig. 1; Wilson, 2003; Cooke et al., 2007; Harris et al., 2014; Fox et al., 2015). The Cadia province has a mineral resource of 8.7 Mt Cu and 43 MOz. Au (2016; www.newcrest.com.au) and includes four porphyry Au-Cu deposits: Cadia Hill, Cadia Quarry, Ridgeway and Cadia East, and two related skarn deposits, Big Cadia and Little Cadia. This Ordovician alkalic porphyry mineralization (ca. 440 Ma; Wilson et al., 2007) is associated with composite monzonite to diorite dykes, plugs and stocks, and some mineralization also occurs locally in the host Forest Reef volcanic rocks. The Cadia Intrusive Complex hosts the Cadia Hill and Cadia Quarry deposits and varies from diorite to quartz monzodiorite, but is dominantly composed of porphyritic monzonite stocks (e.g., the Cadia Hill stock). The Ridgeway deposit, 2.5 km northwest of Cadia Hill, is hosted in monzonites of the Ridgeway Intrusive Complex, and in the Forest Reef volcanics and underlying Weemalla Formation.

Cowal District, Australia

The Cowal Gold mine is located ~40 km northeast of West Wyalong, central New South Wales, Australia (Fig. 1). Here, the Cowal Igneous Complex hosts several Au deposits and prospects, with two dominant mineralization styles: 1) structurally controlled, epithermal-related Au ± Ag mineralization; and 2) bulk-tonnage porphyry Au-Cu (Zukowski, 2014). One of the best-known porphyry deposits is Marsden with an indicated and inferred mineral resource of 180 Mt at 0.38% Cu with 0.20 g/t Au (www.evolutionmining.com.au). The Cowal Igneous Complex is cut by a poorly defined WNW-trending structure, the Marsden lineament, which juxtaposes the volcanic and sedimentary epithermal host rocks to the north with plutonic rocks that host the porphyry Cu-Au deposits to the south.

Northparkes, Australia

The Northparkes district in central western New South Wales (Fig. 1) has current reserves at 107.5 Mt at 0.81% Cu-equivalent grade containing 667 kt Cu (http://www.chinamoly.com). Economic Cu-Au mineralization is associated with discrete alkalic pencil porphyries emplaced in the late Ordovician (~444 – 439 Ma; Lickfold et al., 2003, 2007; Crawford, 2007). Host rocks to porphyry Cu deposits include the 445 – 436 Ma Wombin volcanics, a series of high-K calc-alkaline to shoshonitic volcaniclastic sedimentary rocks and interbedded lavas that along with the Nelungaloo and Goonumbla Volcanics comprise the Goonumbla Volcanic Complex (Heithersay and Walshe, 1995; Lickfold et al., 2003; Lickfold et al., 2007). The Nelungaloo volcanics were intruded by monzodiorite porphyries with sub-economic mineralization at 481 ± 4 Ma (early Ordovician; Simpson et al., 2005; Glen et al., 2007). The Nelungaloo volcanics are overlain by the Goonumbla volcanic complex on a low-angle unconformity (Krynen et al., 1990; Lickfold et al., 2007). A series of basaltic trachyandesite and augite monzonite porphyry dykes post-date mineralization in the Northparkes district (Lickfold, 2003).

Methods

Sources of data for Sr/MnO vs Sr/Y diagram

Conventional whole-rock geochemical data of intrusive rocks (ICP-MS/ICP-ES and XRF) from a wide variety of porphyry settings were compiled from both published work and unpublished PhD theses. Samples included in this dataset were visibly unaltered based on petrographic and field observations made by respective authors. Following the methodology of Loucks (2014), fertile sample suites were selected from representative syn-mineralization intrusive rocks from porphyry and high-sulfidation ore deposits. Districts and associated data were divided into groups based on economic metal content: (1) Cu (the Koloula, Luzon, Frieda River, and Yandera deposits); (2) Cu-Au (the Panguna, Waisoi, Grasberg, Skouries, Bajo de la Alumbrera, and Antapaccay deposits); (3) Cu-Mo (the Bagdad, Ray-Christmas, Safford, El-Teniente; Fujiawu, Tongchang, Tuwu-Yangdong, Baogotu, Zhanaga, Yulong, Malasongduo, Duoxiasongduo, Mongzong, Yerington, Los Pelambres, El Abra, Qulong, Riduo, and El Salvador deposits); (4) Cu-Mo-Au (the Chikang, Cevizlidere, and Altar deposits); and (5) Au (the Shuteen deposit). The comparator barren sample suite is a compilation of data from the Sunda and Surigao arcs and the Collahuasi deposit. The Sunda Arc dataset was selected because it represents a typical mid-crustal thickness arc magma not associated with any known porphyry Cu (or other) mineralization (Soller et al., 1982; Wolbern and Rumpker, 2016).

ICP-MS/ICP-ES

Conventional whole-rock geochemical data from 82 rock chip and drill core samples were evaluated from the six case-study areas (Yerington, Resolution, Las Bambas, Cowal, Cadia and Northparkes). These rock samples were analysed by ICP-MS/ICP-ES for their major and trace element compositions. Samples from each case-study area were analysed separately, as part of larger analytical batches; however analytical methods were consistent between sample batches. Whole-rock geochemical analyses were completed at either Bureau Veritas Mineral Laboratories in Vancouver, Canada, or ALS Laboratories in Perth, Australia. The methods followed at each lab were similar. Bureau Veritas analytical methods are described here. Samples were jaw-crushed, split, and pulverized. The pulverized samples were dried and loss on ignition was determined from changes in sample weight before and after heating. A total of 43 major and trace elements were analysed using lithium borate

fusion package LF200. A 0.2 g powdered sample was fused in a graphite crucible with 1.5 g of $LiBO_2/LiB_4O_7$ flux at 980°C for 30 min and then dissolved in 5% HNO_3. Major elements, including MnO, were determined using a Jarrel Ash AtomComp Model 975/Spectro Ciros Vision inductively coupled plasma emission spectrograph (ICP-ES). Trace elements, including Sr and Y, were analysed using a Perkin-Elmer Elan 6000 or 9000 inductively coupled plasma mass spectrometer (ICP-MS). Laboratory quality assurance and quality control procedures were employed with digested standards run every 68 samples, and a digestion duplicate run every 15 samples, with recalibration of the instrument every 68 samples. Carbon and sulfur contents were measured by Leco analysis.

pXRF workflow

The pXRF data collection workflow used in the current study was modified from Fisher et al. (2014) and follows a two-part process: (1) data collection and (2) data calibration. An Olympus Vanta M series pXRF instrument was used, with a 50 Kv Rh tube (instrument number 801231). All pXRF data was collected in Geochem mode. At the beginning of each analytical session, the pXRF unit was initialized to a calibration disc provided by the unit manufacturer. A series of matrix-matched standards were used for quality assurance and quality control: The Priory monzonite (TAS-MONZ); diorite (TAS-DIOR); Grant Point granite (TAS-GRAN); and dolerite (TAS-BAS). Standards and/or a silica blank were run at a minimum of every 20 analyses, and at the beginning and end of each analytical session. Standard materials were collected from the St. Helens region of Tasmania by Cocker (1971) and prepared at the University of Tasmania. To make the pressed powder standard mounts used in the current study, standard samples were jaw-crushed to <6 mesh diameter. Material was then split and lots of 200 g were pulverised in a tungsten carbide mill to 120 mesh and pressed into 30 cm diameter round mounts.

PXRF data were collected on both loose pulp material (120 mesh) in press cups through propylene film and intact rock slabs. To overcome the natural grain size heterogeneity inherent to rock slabs, three separate analyses were collected on each rock slab sample and averaged. Two to three analyses were collected on pulp material (Appendix B). Averaging of multiple pXRF analyses is routinely applied to overcome the low sampling precision of pXRF data on heterogeneous material (e.g., Potts et al., 1997; Le Vaillant et al., 2014; Holding, 2014; Simandl et al., 2014; Hall et al., 2016). Standard deviation values from the mean (1σ)

were calculated to evaluate the sampling precision of multiple analyses from the same sample. On rock slabs, the X-ray beam was placed on different parts of the same sample. This process is referred to herein as niche sampling. Spot locations were selected to avoid visible alteration, veining, and weathering where present.

Calibrations curves for Sr, Y and MnO were created using regressions of pXRF results on the four matrix matched standards versus conventional ICP-MS/ICP-ES data for the standards to provide correction factors for pXRF data. Two sets of calibration curves were devised to calibrate data collected on different sample media. PXRF data collected directly on rock slabs were calibrated to standards placed directly on the pXRF detector, whereas pXRF data collected on loose pulp material (measured through 4 μm thick propylene film) were calibrated to standards also analysed through 4 μm thick propylene film.

Results

Global compilation of conventional whole-rock data

A compilation of conventional whole-rock data is presented on a diagram of Sr/Y vs Sr/MnO in Figure 2. Samples from the barren Sunda Arc, Surigao and Collahuasi reference suite have low Sr/Y (< 50) and low Sr/MnO (< 13 250) values. Samples of syn-mineralization intrusive rocks have overall higher Sr/Y and Sr/MnO values than samples from intrusions not associated with mineralization (Fig. 2). Correlation between Sr/Y and Sr/MnO values, and the empirical prospectivity of intrusions, defines three fields on the Sr/Y vs. Sr/MnO diagram shown in Fig. 2: (1) prospective; (2) unprospective; and (3) mixed signal. These fields were calculated from the 95th percentile of data associated with ore-forming intrusions (prospective field) and those not associated with known mineralization (unprospective field). Samples from Bajo de la Alumbrera, and some samples from Bayugo, Malasongduo, Mongzong, Baogutu, Koloula, and Batu Hijau plot in the mixed signal field. Two samples of intrusions associated with known porphyry Cu deposits, Resolution and Duoxiasongduo, plot near the upper Sr/MnO boundary of the unprospective field (Fig. 2). All other samples associated with porphyry Cu mineralization plot in the prospective field with high Sr/Y (>50) and high Sr/MnO (> 13 250).

pXRF

Calibration of pXRF data to ICP-MS values

Calibration curves and associated calibration factors for MnO, Sr, and Y based on ICP-MS/ICP-ES data and pXRF data collected on the same standards are presented in Figure 3 and Table 2. The associated ICP-MS/ICP-ES and pXRF data for standards are tabulated in Appendix A. The concentrations of Mn, Sr and Y analysed by pXRF are within 15% of ICP-MS/ICP-ES values for both standards sampled by direct measurement and through propylene film. These values correspond to calibration factors between 0.85 and 1.15 (Table 2). Differences between all pXRF and conventional laboratory datasets are consistently offset, as shown by the R^2 values in each diagram (R^2 = 0.97 – 1; Table 2). High positive correlation values between ICP-MS/ICP-ES and pXRF results for Mn and Sr from this study compare favourably with similar results from Piercey and Devine (R^2 > 0.8; 2014).

Precision and accuracy of pXRF data

All instrument precision data (instrument error) are tabulated in Appendix B. Mean values for the analytical errors associated with pXRF measurements of Sr, Y, and Mn are presented in Table 3. Analytical errors for Sr and Mn are below 2% of the average values of these elements in samples analysed in the current study (Table 3). Yttrium has the highest analytical error (11%; Table 3) due to the low concentrations of Y in some samples, approaching the analytical detection limit of the pXRF (near 1 ppm). Analytical precision was also evaluated by analysing the same spot on a rock slab 10 times (Fig. 4; Table 4). This exercise resulted in a relative standard deviation (RSD) value of 0.9% Mn, 0.4% Sr and 5.9% Y (Table 4).

The sampling precisions of pXRF data on rock slabs and pulp material were evaluated by calculating 1σ error (standard deviation from the mean value of all analyses collected on a sample). These values are listed in Tables 5 and 6. RSD values were calculated to assess the magnitude of variation between multiple analyses on the same sample relative to the mean and are included in Tables 5 and 6. Sampling precision was also evaluated by analysing ten different spots on a single sample (Fig. 4) and calculating the RSD for each element (Table 4). RSD values for Sr, Y and Mn are between 5.5 and 16% (Table 4).

The accuracy of pXRF data was evaluated by calculating the relative difference (RD) between pXRF data (mean value of multiple analyses) and conventional laboratory data for

the same samples. Results are illustrated graphically in Figure 5 and included in Tables 5 and 6. At low values of Sr/Y (<100), there is good correlation between pXRF data from rock slabs and ICP-MS data, whereas at higher Sr/Y values (>100) the pXRF overestimates values by up to 54% (Fig. 5C). For both pulp powders and rock slabs, there is excellent correlation between the Sr/MnO values reported by pXRF and ICP-MS/ICP-ES (R^2 = 0.73 – 0.94; Fig. 5). However, in both cases, the pXRF under-estimates Sr/MnO values relative to conventional whole-rock analytical methods (Fig. 5). Overall, RD values are lower for pXRF data collected on pulp powders compared to intact rock slabs (Fig. 5; Tables 5 and 6).

Relative prospectivity of pre-, syn- and post-mineralization intrusions

The Sr/Y and Sr/MnO values of pre-, syn- and post-mineralization intrusions from each case study area are illustrated in Figure 6. At Yerington, samples of pre- and syn-mineralization igneous rocks plot within the prospective fields on the Sr/MnO vs Sr/Y Cu-prospectivity diagram (Fig. 6A). Samples from the Luhr Hill granite return the overall highest Sr/MnO (>10 000) and Sr/Y values (>100), consistent with its classification as a syn-mineralisation intrusion. Samples of the post-mineralization Shamrock monzonite plot in the 'mixed' prospectivity field; however, these samples returned lower Sr/MnO (<11 000) and Sr/Y (<100) values compared to pre- and syn-mineralization rocks (Fig. 6A).

Two samples of the syn-mineralization Schultz granite from Resolution plot in the prospective field (Sr/MnO >10 000), and one syn-mineralization intrusive sample plots in the unprospective field (Fig. 6B). Two samples of pre-mineralization intrusions plot in the unprospective field. At Las Bambas, syn-mineralization intrusions have higher Sr/MnO (>10 000) and Sr/Y values (90-120), than pre-mineralization samples (Sr/MnO = 2000 – 10 000; Sr/Y <50; Fig. 6C). For the Cadia area, syn-mineralization samples plot wholly within the prospective field (Fig. 6D). Most pre-mineralization samples also plot within the prospective field but at overall lower Sr/MnO values (<10 500; Fig. 6D). Unlike the Yerington and Las Bambas districts, Sr/Y values of syn-mineralization intrusions are variable (Fig. 6A – D). Syn-mineralization samples from Cadia have Sr/Y values between 50 and 80, whereas pre-mineralization intrusions have Sr/Y values ranging from 10 – 100 (Fig. 6D).

Samples from the Cowal district show a similar relationship to other districts (Fig. 6E). Samples of syn-mineralization intrusions plot within the prospective field and pre- and post-mineralization intrusions plot close to or within the unprospective field. Syn-mineralization intrusions from the Cowal district have both elevated Sr/MnO (>10 000) and Sr/Y (>80) compared to pre-, and post-mineralization intrusions. Similarly, syn-mineralization intrusions from Northparkes have high Sr/MnO (>7000) and Sr/Y (>40) relative to pre-mineralization intrusions. There is no overlap between the pre-, syn- and post-mineralization datasets from Las Bambas, Cadia, Cowal or Northparkes (Fig. 6).

Altered rocks

Many samples analysed by pXRF in the current study have been weakly altered to epidote ± albite or contain thin epidote veins (e.g., Fig. 4). To evaluate the potential effects of alteration minerals that commonly occur in the porphyry-distal environment, such as epidote and albite on Sr, Y and Mn values, pXRF data were collected directly on veins and altered rock in two spots on a single sample (Fig. 4; Table 4). Results from these two analyses were significantly different (i.e., standard deviation for Sr = 573 ppm), however mean values for Sr and Y in altered spots were within 17% of mean values for least-altered spots (Table 4).

Discussion

In situ pXRF analysis of coarse-grained rocks

Sampling precision and accuracy

The analytical spot size of the pXRF is approximately 1 cm diameter, and the penetration depth of X-rays into the sample is variable depending on the elements analysed (up to 1.1 cm; Potts et al., 1997). Potts et al. (1997) described sampling precision as variations in the mineral assemblage (typically due to grain size) within the volume of rock analysed by pXRF when replicate measurements are made on different parts of a particular sample. To minimise variability due to sampling precision, we used of average values from three measurements on rock slabs (2 – 3 for pulp powders), following the methods outlined in previous studies (e.g., Le Vaillant et al., 2014; Simandl et al., 2014).

Mean RSD values of Sr/Y and Sr/MnO pXRF data on pulp samples were lower (<7%) than pXRF data collected on intact rock slabs (24 – 32%; Tables 5 and 6). These results indicate that repeat measurements of pulp material return more consistent values than rock slabs. The higher sampling precision of pulp powders is not surprising given the homogeneity of the sample volume, both with respect to grain size and mineralogy. Conversely, intact rock slabs have variable grain size and the distribution of minerals is not uniform across the sample (i.e., Fig. 4). Despite the significant differences between repeat measurements of rock slabs (Table 5), mean values for each sample plot within the expected fields on the Sr/Y vs Sr/MnO prospectivity diagram (Fig. 6). Furthermore, the variability between repeat measurements of the same sample, as measured by 1σ standard deviation values, is less than the differences in Sr/Y and Sr/MnO between syn-mineralization intrusions and other intrusions from the same district (Fig. 6). Where there is overlap between datasets from different groups, such as at Yerington (Fig. 6A), the mean values of each dataset are sufficiently different from one another to assess the relative fertility of each group. Figure 7 illustrates that there is no overlap between the 1σ error bars for mean values of pre- and syn-mineralization intrusive rocks at Yerington, and post-mineralization intrusive rocks, unprospective for porphyry Cu mineralization. There is overlap between Sr/Y and Sr/MnO values of pre- and syn-mineralization intrusions, which can be attributed to the genetic

relationship between different phases of the Yerington batholith, which formed by progressive fractional crystallisation (Dilles, 1987).

In addition to being more precise, pXRF data of pulp material is also more accurate than data of rock slabs relative to conventional ICP-MS and ICP-ES data (Fig. 5; Tables 5 and 6). The mean relative differences between values of Sr/Y and Sr/MnO are lower for pulp material (16% Sr/Y and 19% Sr/MnO; Table 6) than intact rock slabs (78% Sr/Y and 32% Sr/MnO; Table 5). There are two explanations for this. First, samples collected in the field were split by hand. One half of the sample was sent for conventional whole-rock analysis and the other half was used for pXRF analysis. Although split from a single rock mass, the two rock halves are not duplicates. It is therefore not surprising that the whole-rock and pXRF values are not identical given an expected degree of natural heterogeneity between the two sample halves. Another difference between the two methods is that conventional whole-rock sampling analyses the sample in its entirety whereas pXRF data acquisition on rock slabs targeted least-altered parts of the sample. PXRF data of rock slabs may therefore represent the most pristine or unaltered values for a given rock sample whereas conventional data may include some veins and/or weak alteration.

The relative difference between pXRF data of rock slabs and conventional laboratory data is greater for Sr/Y values (78%) than Sr/MnO values (32%; Table 5). This difference is likely due to the low concentration of Y in some samples, particularly where ferromagnesian minerals such as hornblende and biotite are absent or were not analysed by the pXRF. Overall, syn-mineralization intrusions have lower Y values than pre- or post-mineralization intrusions from the same district (Figure 6), and Y values can approach 1 ppm, which is near the detection limit of the pXRF instrument (Appendix B). Manganese and Sr occur in much higher concentrations in all rocks (hundreds of ppm; Appendix B), and are therefore not affected by analytical detection limit issues. In this way, pXRF values of Sr/MnO may be a more robust approximation of whole-rock fertility signatures. Despite the challenges of analytical detection limit, Sr/Y values of syn-mineralization intrusions were still higher overall than pre- or post-mineralization intrusions from the same district.

The potential effects of alteration on prospectivity assessment

Loucks (2014) highlighted the importance of selecting least-altered rocks for Cu-prospectivity analysis due to the mobility of elements such as Sr (and Mn) during alteration associated with porphyry Cu mineralization. However, most porphyry Cu deposits typically have large alteration footprints that can extend kilometres from the deposit centre (Lowell and Guilbert, 1970; Gustafson and Hunt, 1975; Seedorff et al., 2005; Sillitoe, 2010; Cooke et al., 2014), which can make least-altered samples difficult to find. Baldwin and Pearce (1982) used both unaltered and weakly altered samples in their discrimination of productive and unproductive intrusions using MnO and Y. They concluded that the replacement of hornblende by biotite ± ilmenite ± titanite did not affect the classification of a sample as either productive of unproductive.

Some samples from the six porphyry districts presented in the current study were weakly altered to epidote ± albite ± chlorite ± actinolite, common alteration minerals in the porphyry-distal environment (Cooke et al., 2014; Fig. 4). Epidote and albite can incorporate significant amounts of Sr into their crystal structures (Frei et al., 2004). The presence of these minerals (likely in significant quantities) may therefore result in a false positive fertility signature on the Sr/Y vs Sr/MnO fertility diagram if they are analysed in the sample volume excited by the pXRF. This kind of false positive was highlighted in the current study (Table 4), where one analysis that included an epidote vein yielded nearly 400 ppm more Sr than least-altered parts of the same sample. False positives can be mitigated, at least in part, by selecting the least-altered part of a rock sample for pXRF analyses (Fig. 4).

Calibration curves

The ICP-MS/pXRF calibration curves applied in this study used data collected on pulverized standard material prepared in press cups. PXRF analysis of press cup material presents a smooth uniform surface to the pXRF, enabling complete contact between the instrument and the sample surface. Futhermore, the rock material has been homogenised into a very fine-grained powder (120 mesh) decreasing the effects of mineral and grain size heterogeneity. Ideally, all samples would be presented to the pXRF in this way, as it has been demonstrated in the current study that pXRF data on pulp powders return more accurate results than rock slabs (Fig. 5; Tables 5 and 6). However, field applications present

less ideal and more variable sample surface geometries and coarser grain sizes, making sample presentation an issue that can affect data quality (Young et al., 2016). Given that we calibrated pXRF data of coarse-grained rock slabs using calibration factors derived from standards in pressed powder mounts, there is the potential for unforeseen mineral matrix effects to affect these data due to differences in the relative proportions of minerals present in the rock slab and standard material. Unfortunately, the heterogeneity of medium to coarse-grained rock slabs makes developing a matrix matched standard nearly impossible.

Implications for exploration

The whole-rock geochemical compilation (ICP-MS/ICP-ES; XRF) of nearly 30 porphyry Cu districts from the current study shows that Sr/Y and Sr/MnO values can be used to discriminate between prospective and unprospective intrusions (Fig. 2). However, there is overlap between the prospective and unprospective datasets. This overlap is consistent with other published studies that also assessed the ore-forming potential of intrusions, which show significant overlap in the values of key element fertility indicators between unmineralized and mineralized suites (Fig. 2; Baldwin and Pearce, 1982; Loucks, 2014; Dilles et al., 2015; Lu et al., 2016), especially for porphyry Cu and porphyry Cu-Mo suites generated in thick crust Andean-type environments.

Overlap between prospective and unprospective datasets from the conventional whole-rock prospectivity diagram (Fig. 2) are consistent with pXRF results of intrusive rocks from the six case study areas (Fig. 6). Overall, the relative prospectivity of each intrusion from the six case study areas correlates with its temporal relationship to mineralization (Fig. 6). Samples of pre- and post-mineralization intrusions, unprospective for porphyry Cu formation, return lower Sr/Y and Sr/MnO values than syn-mineralization intrusions. However, the absolute values of Sr/Y and Sr/MnO that separate prospective and unprospective intrusions vary between districts (Fig. 6). Here, we propose that while global reference suites should continue to be used to understand the general relationship between mineralized and unmineralized intrusions, as has been done in the current study, they should not be used to develop hard numerical boundaries that define the ore-forming potential of an intrusion—this needs to be treated on a district by district basis. The use of a global set of numerical prospectivity boundaries may lead to false positive classifications of unprospective intrusions or conversely, misclassification of fertile intrusions as unprospective. The method

outlined in the current study is therefore best applied in regional exploration, where there is some pre-existing knowledge of background Sr/Y and Sr/MnO values.

The benefits of pXRF data acquisition

We have identified four benefits of using pXRF data to inform Cu prospectivity diagrams, rather than conventional ICP-MS or XRF methods. First is cost; although purchase of a pXRF instrument requires an initial cost, there is no limit to the number of analyses collected following purchase. This makes the cost of a single pXRF analysis one or two orders of magnitude lower than whole-rock geochemical analyses from a commercial laboratory. Second is time; a single pXRF analysis can be collected in around 90 seconds. Third is the volume of data; the speed with which pXRF data can be collected permits multiple analyses to be collected for a single sample and many samples to be analysed from a single lithological unit. Larger sample populations allow for better statistics to be performed on the dataset and for increased confidence in an individual intrusion plotting as either prospective or unprospective. The fourth and final benefit of pXRF data acquisition in this context is niche sampling. Data collection using pXRF permits the user to target the least-altered parts of an outcrop or hand sample (Fig. 4). Together, the four benefits of pXRF data collection support rapid, low-cost data collection in the field that can result in real-time decision making about the prospectivity of intermediate to felsic rocks in a given exploration search space.

Conclusions

A global compilation of conventional whole-rock geochemical data from a wide variety of porphyry Cu settings shows that ore-forming intrusive rocks have higher Sr/Y and Sr/MnO values than an unprospective suite of rocks (Fig. 2). Higher Sr/Y and Sr/MnO proportions are interpreted to reflect the combined processes of hornblende fractionation and plagioclase suppression in hydrous melts, characteristic of ore-forming intrusions (Baldwin and Pearce, 1982; Defant and Drummond, 1990; Richards and Kerrich, 2009; Richards, 2011; Loucks, 2014).

ICP-MS/ICP-ES calibrated pXRF data collected on both pulp powders and intact rock slabs from six globally significant porphyry districts highlight how the binary plot of Sr/Y vs Sr/MnO can be applied to rapidly identify the ore-forming potential of an intrusive rock in the field (Fig. 6). PXRF data of syn-mineralization intrusive rocks have higher mean values of Sr/Y and Sr/MnO relative to pre- and/or post-mineralization intrusions from the same district (Fig. 6). Although there is variability between multiple pXRF analyses collected on an individual intact rock slab, this variation is less than the variation in Sr/Y and Sr/MnO values between pre-, syn- and post mineralization intrusions from the same district (Fig. 7). Portable XRF instruments represent a rapid and cost-effective method to collect Sr, Mn and Y data to assess the ore-forming potential of intrusions.

Acknowledgments

This research is part of a PhD project funded by the AMIRA International P1153 project 'Applying the explorer's toolbox to discover Cu, Au, and Mo deposits', an Australian Postgraduate Award, and an AusIMM Education Endowment Fund scholarship. It was also supported by the ARC Research Hub for Transforming the Mining Value Chain. Many thanks to Jay Thompson, manager of the pXRF laboratory facilities at the University of Tasmania. All samples analysed by pXRF were collected as part of the PhD field research of the authors of this study (Yerington, Cowal, Resolution, Las Bambas, Northparkes), or with the permission of the owners of the samples. Thanks to Tim Ireland (Collahuasi) and Alan Wilson (Cadia) for providing their samples and associated whole-rock geochemical data for this study. Sincere thanks to Matt Cunningham of Hudbay Minerals (formerly Mason Resources), George Eliopolous and Todd Bonsall from Quaterra Resources, and Rana Gill and Hank Ohlin from Mason Valley Copper for property access, drill core access, and geological discussions in the field in the Yerington district area. We are grateful to Dr Stephen Piercey and an anonymous reviewer for their comments and suggestions, all of which greatly improved the paper.

References

Anthony, E.Y., and Titley, S.R., 1988, Progressive mixing of isotopic reservoirs during magma genesis at the Sierrita porphyry copper deposit, Arizona: Inverse solutions: Geochimica et Cosmochimica Acta, v. 52, p. 2235-2249.

Bachmann, O., Dungan, M.A., Bussy, F., 2005, Insights into shallow magmatic processes in large silicic magma bodies: The trace element record in the Fish Canyon magma body, Colorado: Contributions to Mineralogy and Petrology, v. 149, p. 338–349.

Baker, M.J., Hollings, P., Thompson, J.A., Thompson, J.M., and Burge, C., 2016, Age and geochemistry of host rocks of the Cobre Panama porphyry Cu–Au deposit, central Panama: Implications for the Paleogene evolution of the Panamanian magmatic arc: Lithos, v. 248, p. 40–54.

Ballantyne, G., Marsh, T., Hehnke, C., Andrews, D., Eichenlaub, A., and Krahulec, K., 2003, The Resolution copper deposit, a deep, high-grade porphyry copper deposit in the Superior district, Arizona: Marco T. Einaudi Symposium, Colorado school of Mines, 2003, Colorado, USA, 12 p.

Ballard, J.R., Palin, M.J., and Campbell, I.H., 2002, Relative oxidation states of magmas inferred from Ce (IV)/Ce (III) in zircon: Application to porphyry copper deposits of northern Chile: Contributions to Mineralogy and Petrology, v. 144, p. 347–364.

Baldwin, J., and Pearce, J.A., 1982, Discrimination of productive and nonproductive porphyritic intrusions in the Chilean Andes: Economic Geology, v. 77, p. 664–674.

Banik, T.J., Coble, M.A., and Miller, C.F., 2017, Porphyry Cu formation in the middle Jurassic Yerington batholith, Nevada, USA: Constraints from laser Raman, trace element, U-Pb age, and oxygen isotope analyses of zircon: Geosphere, v. 13, p. 1113–1132.

Batkhishig, B., Noriyoshi, T., and Greg, B., 2010, Magmatism of the Shuteen Complex and Carboniferous subduction of the Gurvansaikhan terrane, South Mongolia: Journal of Asian Earth Sciences, v. 37, p. 399–411.

Boon, K.A. and Ramsey, M.H., 2012, Judging the fitness of on-site measurements by their uncertainty, including the contribution from sampling: Science of the Total Environment, v. 419, p. 196–207.

Brand, N., and Brand, C., 2014, Performance comparison of portable XRF instruments: Geochemistry: Exploration, Environment, Analysis, v. 14, p. 125–138.

Braxton, D.P., 2007, Boyongan and bayugo porphyry copper-gold deposits NE Mindanao, Philippines: Geology, geochemistry, and tectonic evolution: Unpublished P.hD. thesis, Hobart, Australia, University of Tasmania, 279 p.

Cannell, J., Cooke, D.R., Walshe, J.L., and Stein, H., 2005, Geology, mineralization, alteration, and structural evolution of the El Teniente porphyry Cu-Mo deposit: Economic Geology, v. 100, p. 979–1003.

Carr, R., Zhang, C., Moles, N., and Harder, M., 2008, Identification and mapping of heavy metal pollution in soils of a sports ground in Galway City, Ireland, using a portable XRF analyser and GIS: Environmental Geochemistry and Health, v. 30, p. 45–52.

Castillo, P.R., Janney, P.E., Solidum, R., 1999, Petrology and geochemistry of Camiguin Island, southern Philippines: Insights into the source of adakite and other lavas in a complex arc tectonic setting: Contributions to Mineralogy and Petrology, v. 134, p. 33–51.

Chivas, A.R., 1978, Porphyry copper mineralization at the Koloula igneous complex, Guadalcanal, Solomon Islands: Economic Geology, v. 73, p. 645–677.

Cocker, H.A., Valente, D.L., Park, J.-W., and Campbell, I.H., 2015, Using platinum group elements to identify sulfide saturation in a porphyry Cu system: The El Abra porphyry Cu deposit, Northern Chile: Journal of Petrology, v. 56, p. 2491–2514.

Cocker, J.D., 1971: The St. Helens pluton petrology and structure: Unpublished honours thesis, Hobart, Australia, University of Tasmania

Cooke, D.R., Hollings, P., and Walshe, J.L., 2005, Giant porphyry deposits: Characteristics, distribution, and tectonic controls: Economic Geology, v. 100, p. 801–818.

Cooke, D.R., Wilson, A.J., House, M.J., Wolfe, R.C., Walshe, J.L., Lickfold, V., and Crawford, A.J., 2007, Alkalic porphyry Au-Cu and associated mineral deposits of the Ordovician to Early Silurian Macquarie Arc, New South Wales: Australian Journal of Earth Sciences, v. 54, p. 445–463.

Cooke, D.R., Hollings P., Wilkinson J.J., and Tosdal R.M., 2014, Geochemistry of porphyry deposits: Treatise on Geochemistry, 2nd ed., v. 13, p. 357−381.

Costa, F., Scaillet, B., and Pichanvant, M., 2004, Petrological and experimental constraints on the pre-eruption conditions of Holocene dacite from Volcan San Pedro (36°S, Chilean Andes) and the importance of sulphur in silicic subduction-related magmas. Journal of Petrology, v. 45, p. 855–881.

Drummond, M.S., and Defant, M.J., 1990, A model for trondhjemite-tonalite-dacite genesis and crustal growth via slab melting: Archean to modern comparison: Journal of Geophysical Research, Solid Earth, v. 95, p. 21503 – 21521.

Dilles, J.H., and Einaudi, M.T., 1992, Wall-rock alteration and hydrothermal flow paths about the Ann-Mason porphyry copper deposit, Nevada; a 6-km vertical reconstruction: Economic Geology, v. 87, p. 1963–2001.

Dilles, J.H., and Wright, J.E., 1988, The chronology of early Mesozoic arc magmatism in the Yerington district of western Nevada and its regional implications: Geological Society of America Bulletin, v. 100, p. 644–652.

Dilles, J. H., 1987, Petrology of the Yerington Batholith, Nevada; evidence for evolution of porphyry copper ore fluids: Economic Geology, v. 82, p. 1750–1789.

Drummond, M.S., Defant, M.J. and Kepezhinskas, P.K., 1996. Petrogenesis of slab-derived trondhjemite–tonalite–dacite/adakite magmas: Earth and Environmental Science Transactions of the Royal Society of Edinburgh, v. 87, p. 205–215.

Duée, C., Orberger, B., Maubec, N., Laperche, V., Capar, L., Bourguignon, A., Bourrat, X., El Mendili, Y., Chateigner, D., and Gascoin, S., 2019, Impact of heterogeneities and surface roughness on pXRF, pIR, XRD and Raman analyses: Challenges for on-line, real-time combined mineralogical and chemical analyses on drill cores and implication for "high speed" Ni-laterite exploration: Journal of Geochemical Exploration, v. 198, p. 1–17.

Durance, P, Jowitt, S. M., and Bush, K., 2014, An assessment of portable X-ray fluorescence spectroscopy in mineral exploration, Kurnalpi Terrane, Eastern Goldfields Superterrane, Western Australia: Applied Earth Science, Transactions of the Institutions of Mininga nd Metallurgy: Section B, v. 123, p. 150–163.

Einaudi, M.T., 1977, Petrogenesis of the copper-bearing skarn at the Mason Valley Mine, Yerington District, Nevada: Economic Geology, v. 72, p. 769–795.

Fisher, L., Gazley, M.F., Baensch, A., Barnes, S. J., Cleverley, J., and Duclaux, G., 2014, Resolution of geochemical and lithostratigraphic complexity: A workflow for application of portable X-ray fluorescence to mineral exploration: Geochemistry: Exploration, Environment, Analysis, v. 14, p. 149–159.

Ford, J., 1976, A geochemical and stable isotope study of the Panguna porphyry copper deposit, Bougainville: Unpublished Ph. D. thesis, Brisbane, Australia, University of Queensland, 213 p.

Fox, N., Cooke, D.R., Harris, A.C., Collett, D., and Eastwood, G., 2015, Porphyry Au-Cu mineralization controlled by reactivation of an arc-transverse volcanosedimentary subbasin: Geology, v. 43, p. 811–814.

Frei, R., 1995, Evolution of mineralizing fluid in the porphyry copper system of the Skouries Deposit, Northeast Chalkidiki (Greece); evidence from combined Pb-Sr and stable isotope data: Economic Geology, v. 90, p. 746–762.

Gazley, M.F., Vry, J.K., du Plessis, E., Handler, M.R., 2011. Application of hand-held X-ray fluorescence analyses to Metabasalt Stratigraphy, Plutonic Gold Mine, Western Australia. J. Geochem. Explor. 110, 74–80.

Gazley, M., and Fisher, L., 2014, A review of the reliability and validity of portable X-ray fluorescence spectrometry (pXRF) data: Mineral Resource and Ore Reserve Estimation–The AusIMM Guide to Good Practice, p. 69–82.

Gazley, M.F., Tutt, C.M., Fisher, L.A., Latham, A.R., Duclaux, G., Taylor, M.D., and de Beer, S.J., 2014, Objective geological logging using portable XRF geochemical multi-element data at Plutonic Gold Mine, Marymia Inlier, Western Australia: Journal of Geochemical Exploration, v. 143, p. 74–83.

Gazley, M.F., Duclaux, G., Fisher, L.A., de Beer, S., Smith, P., Taylor, M., Swanson, R., Hough, R.M., Cleverley, J., 2012, Improving geological and metallurgical understanding of Plutonic Gold Mine, Western Australia, using 3-D visualisation of portable X- ray fluorescence data, Applied Earth Science, Transactions of the Institute of Materials, Minerals and Mining, v. 120, 88–96.

Glen, R., Crawford, A., and Cooke, D., 2007, Tectonic setting of porphyry Cu–Au mineraliation in the Ordovician–Early Silurian Macquarie Arc, Eastern Lachlan Orogen, New South Wales: Australian Journal of Earth Sciences, v. 54, p. 465–479.

Green, T.H., and Pearson, N.J., 1985, Experimental determination of REE partition coefficients between amphibole and basaltic to andesitic liquids at high pressure: Geochimica et Cosmochimica Acta, v. 49, p. 1465–1468

Greenland, L.P., Gottfried, D., and Tilling, R.I., 1968, Distribution of manganese between coexisting biotite and hornblende in plutonic rocks: Geochimica et Cosmochimica Acta, v. 32, p. 1149–1163.

Goodale, N., Bailey, D.G., Jones, G.T., Prescott, C., Scholz, E., Stagliano, N., and Lewis, C., 2012, pXRF: A study of inter-instrument performance: Journal of Archaeological Science, v. 39, p. 875–883.

Gustafson, L.B., and Hunt, J.P., 1975, The porphyry copper deposit at El Salvador, Chile: Economic Geology, v. 70, p. 857–912.

Hammer, D.F., 1972, Geological investigation of the Superior area, Pinal County, Arizona: Unpublished report prepared for the Magma Copper Company by Newmont Exploration Limited, 56 p.

Harris, N.B., and Einaudi, M.T., 1982, Skarn deposits in the Yerington District, Nevada; metasomatic skarn evolution near Ludwig: Economic Geology, v. 77, p. 877–898.

Harris, A.C., Percival, I.G., Cooke, D.R., Tosdal, R.M., Fox, N., Allen, C.M., Tedder, I., McMillan, C., Dunham, P., and Collett, D., 2014, Marine volcanosedimentary basins hosting porphyry Au-Cu deposits, Cadia Valley, New South Wales, Australia: Economic Geology, v. 109, p. 1117–1135.

Heithersay, P.S., and Walshe, J.L., 1995, Endeavour 26 North; a porphyry copper-gold deposit in the Late Ordovician, shoshonitic Goonumbla volcanic complex, New South Wales, Australia: Economic Geology, v. 90, p. 1506–1532.

Holding, M.C., 2014, Improved field hXRF analysis - The critical role of representative training set selection (geology), spectral acquisition (sensor sampling), proper calibration/validation (chemometrics): Unpublished B.Sc. thesis, Copenhagen, Denmark, University of Copenhagen, 110 p.

Hollings, P., Wolfe, R., Cooke, D.R., and Waters, P.J., 2011, Geochemistry of Tertiary igneous rocks of northern Luzon, Philippines: Evidence for a back-arc setting for alkalic porphyry copper-gold deposits and a case for slab roll-back?: Economic Geology, v. 106, p. 1257–1277.

Hu, Y.-B., Liu, J.-Q., Ling, M.-X., Ding, W., Liu, Y., Zartman, R.E., Ma, X.-F., Liu, D.-Y., Zhang, C.-C., and Sun, S.-J., 2015, The formation of Qulong adakites and their relationship with porphyry copper deposit: geochemical constraints: Lithos, v. 220, p. 60–80.

Imai, A., Ohbuchi, Y., Tanaka, T., Morita, S., and Yasunaga, K., 2007, Characteristics of porphyry Cu mineralization at Waisoi (Namosi district), Viti Levu, Fiji: Resource geology, v. 57, p. 374–385.

Imai, A., 2002, Metallogenesis of Porphyry Cu Deposits of the Western Luzon Arc, Philippines: K- Ar ages, SO3 Contents of Microphenocrystic Apatite and Significance of Intrusive Rocks: Resource Geology, v. 52, p. 147–161.

İmer, A., Richards, J.P., Creaser, R.A., and Spell, T.L., 2015, The late Oligocene Cevizlidere Cu-Au-Mo deposit, Tunceli Province, eastern Turkey: Mineralium Deposita, v. 50, p. 245–263.

Jiang, Z., Wang, Q., Wyman, D.A., Shi, X., Yang, J., Ma, L., and Gou, G., 2015, Zircon U–Pb geochronology and geochemistry of Late Cretaceous–Early Eocene granodiorites in the southern Gangdese batholith of Tibet: Petrogenesis and implications for geodynamics and Cu±Au±Mo mineralization: International Geology Review, v. 57, p. 373–392.

Krynen, J., Sherwin, L., and Clarke, I., 1990, Stratigraphy and structure: Geological setting of gold and copper deposits in the Parkes area, New South Wales, p. 3–76.

Kulla, G., Oshust, P., Desautels, J.R.P., Melnyk, J., Zurowski, G., Jones, L., and Colantonio, M., 2015, Updated preliminary economic assessment on the Ann Mason project Nevada, U.S.A, AMEC Foster Wheeler Americas Ltd., 361p.

Lang, J.R., and Titley, S.R., 1998, Isotopic and geochemical characteristics of Laramide magmatic systems in Arizona and implications for the genesis of porphyry copper deposits: Economic Geology, v. 93, p. 138–170.

Lemière, B., 2015, Field Analytical Techniques for Geochemical Surveys: 27th International Applied Geochemistry Symposium, April 2015, Tucson, Arizona, United States. 5 p.

Lemière, B., 2018, A review of pXRF (field portable X-ray fluorescence) applications for applied geochemistry: Journal of Geochemical Exploration, v. 188, p. 350-363.

Le Vaillant, M., Barnes, S.J., Fisher, L., Fiorentini, M.L. and Caruso, S. (2014) Use and calibration of portable X-Ray fluorescence analysers: application to lithogeochemical exploration for komatiite-hosted nickel sulphide deposits: Geochemistry: Exploration, Environment, Analysis 14, 199–209.

Lickfold, V., Cooke, D.R., Crawford, A.J., and Fanning, C., 2007, Shoshonitic magmatism and the formation of the Northparkes porphyry Cu–Au deposits, New South Wales: Australian Journal of Earth Sciences, v. 54, p. 417–444.

Loucks, R., 2014, Distinctive composition of copper-ore-forming arcmagmas: Australian Journal of Earth Sciences, v. 61, p. 5–16.

Lowell, J.D., and Guilbert, J.M., 1970, Lateral and vertical alteration-mineralization zoning in porphyry ore deposits: Economic Geology, v. 65, p. 373–408.

McMahon, T.P., 1994, Pliocene intrusions in the Gunung Bijih (Ertsberg) mining district, Irian Jaya, Indonesia: Petrography and mineral chemistry: International Geology Review, v. 36, p. 820–849.

Maher, D., 2008, Reconstruction of middle Tertiary extension and Laramide porphyry copper systems, east-central Arizona: Unpublished Ph.D. thesis, Arizona, USA, University of Arizona, 330p.

Mason, D., and McDonald, J., 1978, Intrusive rocks and porphyry copper occurrences of the Papua New Guinea-Solomon Islands region; a reconnaissance study: Economic Geology, v. 73, p. 857–877.

Mauriohooho, K., Barker, S.L., and Rae, A., 2016, Mapping lithology and hydrothermal alteration in geothermal systems using portable X-ray fluorescence (pXRF): A case study from the Tauhara geothermal system, Taupo Volcanic Zone: Geothermics, v. 64, p. 125–134.

Maydagán, L., Franchini, M., Chiaradia, M., Dilles, J., and Rey, R., 2014, The Altar porphyry Cu-(Au-Mo) deposit (Argentina): A complex magmatic-hydrothermal system with evidence of recharge processes: Economic Geology, v. 109, p. 621–641.

Mungall, J.E., 2002, Roasting the mantle: Slab melting and the genesis of major Au and Au-rich Cu deposits: Geology, v. 30, p. 915–918.

Perelló, J., Carlotto, V.C., Zárate, A., Ramos, P., Posso, H.C., Neyra, C., Caballero, A., Fuster, N.S., and Muhr, R., 2003, Porphyry-style alteration and mineralization of the middle Eocene to early Oligocene Andahuaylas-Yauri belt, Cuzco region, Peru: Economic Geology, v. 98, p. 1575–1605.

Piercey, S.J., and Devine, M.C., 2014, Analysis of powdered reference materials and known samples with a benchtop, field portable X-ray fluorescence (pXRF) spectrometer: Evaluation of performance and potential applications for exploration lithogeochemistry: Geochemistry: Exploration, Environment, Analysis, v. 14, p. 139–148.

Potts, P.J., Williams-Thorpe, O., and Webb, P.C., 1997, The bulk analysis of silicate rocks by portable X-ray fluorescence: effect of sample mineralogy in relation to the size of the excited volume: Geostandards Newsletter, v. 21, p. 29–41.

Proffett, J.M., and Dilles, J.H., 1984, Geologic map of the Yerington district, Nevada: Nevada Bureau of Mines and Geology, map 77.

Reich, M., Parada, M.A., Palacios, C., Dietrich, A., Schultz, F., and Lehmann, B., 2003, Adakite-like signature of Late Miocene intrusions at the Los Pelambres giant porphyry copper deposit in the Andes of central Chile: Metallogenic implications: Mineralium deposita, v. 38, p. 876–885.

Richards, J.P., Boyce, A.J., and Pringle, M.S., 2001, Geologic evolution of the Escondida area, northern Chile: A model for spatial and temporal localization of porphyry Cu mineralization: Economic Geology, v. 96, p. 271–305.

Richards, J.P., and Kerrich, R., 2007, Special paper: Adakite-like rocks: Their diverse origins and questionable role in metallogenesis: Economic geology, v. 102, p. 537–576.

Richards, J.P., 2011, High Sr/Y arc magmas and porphyry Cu±Mo±Au deposits: Just add water: Economic Geology, v. 106, p. 1075–1081.

Richards, J.P., Spell, T., Rameh, E., Razique, A., and Fletcher, T., 2012, High Sr/Y magmas reflect arc maturity, high magmatic water content, and porphyry Cu±Mo±Au potential: Examples from the Tethyan arcs of central and eastern Iran and western Pakistan: Economic Geology, v. 107, p. 295–332.

Rooney, T.O., Franceschi, P., Hall, C.M., 2011, Water-saturated magmas in the Panama Canal region: A precursor to adakite-like magma generation?: Contributions to Mineralogy and Petrology, v. 161, p. 373–388.

Ryan, J., Shervais, J., Li, Y., Reagan, M., Li, H., Heaton, D., Godard, M., Kirchenbaur, M., Whattam, S., and Pearce, J., 2017, Application of a handheld X-ray fluorescence spectrometer for real-time, high-density quantitative analysis of drilled igneous rocks and sediments during IODP Expedition 352: Chemical Geology, v. 451, p. 55–66.

Seedorff, E., Dilles, J., Proffett, J., Einaudi, M., Zurcher, L., Stavast, W., Johnson, D., and Barton, M., 2005, Porphyry deposits: characteristics and origin of hypogene features: Economic Geology 100th anniversary volume, v. 29, p. 251–298.

Sellés, D., Ireland, T., Gardeweg, M., Arcos, R., Pino, H., Camacho, J., Sprohnle, C., Sanhueza, A., and Mont, A., 2009, Magmatismo Paleozoico a Reciente en el área de Collahuasi y características geoquímicas de los magmas asociados a mineralización: Santiago, v. 22, p. S11_044.

Shackley, M.S., 2010, Is there reliability and validity in portable X-ray fluorescence spectrometry (PXRF): The SAA Archaeological Record, v. 10, p. 17–20.

Shen, P., Shen, Y., Liu, T., Meng, L., Dai, H., and Yang, Y., 2009, Geochemical signature of porphyries in the Baogutu porphyry copper belt, western Junggar, NW China: Gondwana Research, v. 16, p. 227–242.

Sillitoe, R.H., 2010, Porphyry copper systems: Economic Geology, v. 105, p. 3–41.

Simandl, G.J., Fajber, R., and Paradis, S., 2014, Portable X-ray fluorescence in the assessment of rare earth element enriched sedimentary phosphate deposits: Geochemistry: Exploration, Environment, Analysis, v. 14, p. 211–221.

Simpson, C., Cas, R., and Arundell, M., 2005, Volcanic evolution of a long-lived Ordovician island-arc province in the Parkes region of the Lachlan Fold Belt, southeastern Australia: Australian Journal of Earth Sciences, v. 52, p. 863–886.

Simpson III, R.L., Bock, C.L. and Robbat Jr., A., 1999, Dynamic workplans and field analytics: Metals assessment by inductively coupled plasma/optical emission spectroscopy, Remediation Journal, v. 9, p. 65–78.

Sisson, T.W., 1994, Hornblende-melt trace-element partitioning measured by ion microprobe: Chemical Geology, v. 117, 331–344.

Soller, D.R., Ray, R.D., and Brown, R.D., 1982, A new global crustal thickness map: Tectonics, v. 1, p. 125–149.

Stavast, W.J., 2006, Three-dimensional evolution of magmatic hydrothermal systems, Schultze granite and Ruby Star granodiorite, Arizona: Unpublished Ph.D. thesis, Arizona, USA, University of Arizona, 414 p.

Stöckli, R., 2004, November, Blue Marble next generation, November 1, 2004, NASA Earth Observatory.

Stolz, A., Varne, R., Davies, G., Wheller, G., and Foden, J., 1990, Magma source components in an arc-continent collision zone: The Flores-Lembata sector, Sunda arc, Indonesia: Contributions to Mineralogy and Petrology, v. 105, p. 585–601.

Sun, W.-D., Liang, H.-Y., Ling, M.-X., Zhan, M.-Z., Ding, X., Zhang, H., Yang, X.-Y., Li, Y.., Ireland, T.R., and Wei, Q.-R., 2013, The link between reduced porphyry copper deposits and oxidized magmas: Geochimica et Cosmochimica Acta, v. 103, p. 263–275.

Thiéblemont, D., Stein, G., Lescuyer, J.L., 1997, Epithermal and porphyry deposits: The adakite connection: Comptes Rendus de l'Académie des Sciences, v. 325, p. 103–109.

Ulrich, T., and Heinrich, C.A., 2001, Geology and alteration geochemistry of the porphyry Cu-Au deposit at Bajo de la Alumbrera, Argentina: Economic Geology, v. 96, p. 1719–1742.

Vry, V., Wilkinson, J., Seguel, J., and Millán, J., 2010, Multistage intrusion, brecciation, and veining at El Teniente, Chile: Evolution of a nested porphyry system: Economic Geology, v. 105, p. 119–153.

Wang, Q., Xu, J.-F., Jian, P., Bao, Z.-W., Zhao, Z.-H., Li, C.-F., Xiong, X., and Ma, J.-L., 2005, Petrogenesis of adakitic porphyries in an extensional tectonic setting, Dexing, South China: Implications for the genesis of porphyry copper mineralization: Journal of Petrology, v. 47, p. 119–144.

Watmuff, G., 1978, Geology and alteration-mineralization zoning in the central portion of the Yandera porphyry copper prospect, Papua New Guinea: Economic Geology, v. 73, p. 829–856.

Whalen, J.B., Britten, R.M., and McDougall, I., 1982, Geochronology and geochemistry of the Frieda River prospect area, Papua New Guinea: Economic Geology, v. 77, p. 592–616.

Wheller, G.E., 1986, Petrogenesis of Batur caldera, Bali, and the geochemistry of Sunda-Banda arc basalts: Unpublished Ph.D. thesis, Hobart, Australia, University of Tasmania, 375 p.

Wheller, G., and Varne, R., 1986, Genesis of dacitic magmatism at Batur volcano, Bali, Indonesia: Implications for the origins of stratovolcano calderas: Journal of Volcanology and Geothermal Research, v. 28, p. 363–378.

Whitford, D., 1975, Strontium isotopic studies of the volcanic rocks of the Saunda arc, Indonesia, and their petrogenetic implications: Geochimica et Cosmochimica Acta, v. 39, p. 1287–1302.

Whitford, D.J., White, W.M., and Jezek, P.A., 1981, Neodymium isotopic composition of Quaternary island arc lavas from Indonesia: Geochimica et Cosmochimica Acta, v. 45, p. 989–995.

Wilson, A., 2003, The genesis and exploration context of porphyry copper-gold deposits in the Cadia district, NSW: Unpublished Ph.D. thesis, Hobart, Australia, University of Tasmania, 334 p.

Wilson, A.J., Cooke, D.R., Stein, H.J., Fanning, C.M., Holliday, J.R., and Tedder, I.J., 2007, U-Pb and Re-Os geochronologic evidence for two alkalic porphyry ore-forming events in the Cadia district, New South Wales, Australia: Economic Geology, v. 102, p. 3–26.

Wölbern, I., and Rümpker, G., 2016, Crustal thickness beneath Central and East Java (Indonesia) inferred from P receiver functions: Journal of Asian Earth Sciences, v. 115, p. 69–79.

Yang, L., Deng, J., Guo, C., Zhang, J., Jiang, S., Gao, B., Gong, Q., and Wang, Q., 2009, Ore-forming fluid characteristics of the Dayingezhuang gold deposit, Jiaodong gold province, China: Resource geology, v. 59, p. 181–193.

Young, K.E., Evans, C.A., Hodges, K.V., Bleacher, J.E., and Graff, T.G., 2016, A review of the handheld X-ray fluorescence spectrometer as a tool for field geologic investigations on Earth and in planetary surface exploration: Applied Geochemistry, v. 72, p. 77–87.

Zengqian, H., Hongwen, M., Zaw, K., Yuquan, Z., Mingjie, W., Zeng, W., Guitang, P., and Renli, T., 2003, The Himalayan Yulong porphyry copper belt: Product of large-scale strike-slip faulting in eastern Tibet: Economic Geology, v. 98, p. 125–145.

Zhang, L., Xiao, W., Qin, K., and Zhang, Q., 2006, The adakite connection of the Tuwu–Yandong copper porphyry belt, eastern Tianshan, NW China: Trace element and Sr-Nd-Pb isotope geochemistry: Mineralium Deposita, v. 41, p. 188–200.

Zhu, Y., Weindorf, D.C., and Zhang, W., 2011, Characterizing soils using a portable X-ray fluorescence spectrometer: 1. Soil texture: Geoderma, v. 167, p. 167–177.

Zukowski, W., 2010, Geology and mineralisation of the Endeavour 41 gold deposit, Cowal district, NSW, Australia: Unpublished Ph.D. thesis, Hobart, Australia, University of Tasmania, 287p.

Figure captions

Figure 1. World map showing the locations of case study districts included in this study: (1) Yerington porphyry Cu (±Mo-Au) district, USA; (2) Resolution porphyry Cu-Mo deposit, USA; (3) Las Bambas, Cu-Fe skarn district Peru; (4) Cadia Cu-Au district, Australia; (5) Northparkes Cu-Au district, Australia; and (6) Cowal Cu-Au district, Australia. Map URL: https://eoimages.gsfc.nasa.gov/images/imagerecords/74000/74167/world.200410.3x5400x2700.jpg Photo credit: Stöckli (2004).

Figure 2. Whole-rock geochemical data compilation of samples from barren (pre-, or post-mineralization intrusions) and syn-mineralization intrusions from porphyry Cu (±Mo-Au) deposits. Three prospectivity fields are shown: prospective (associated with porphyry Cu, skarn, or epithermal mineralization); unprospective (pre- or post-mineralization intrusions, or not associated with any known porphyry Cu, skarn, or epithermal mineralization, and mixed signal (overlap between prospective and unprospective fields). Fields were calculated based on the 95th percentile of data for the fertile and barren datasets respectively. Altar: Maydagan et al. (2014); Bagdad: Lang and Titley (1998); Bajo de la Alumbrera: Ulrich and Heinrich (2001); Baogutu: Shen et al. (2009); Batu Hijau: Garwin (2001); Bayugo: Braxton (2007); Luzon: Imai (2002); Hedenquist et al. (1998); Boyongan: Braxton (unpublished data); Cevizlidere: Imer (2014); Chikang: Jiang et al. (2015); Collahuasi: Selles et al. (2009); Copper Basin: Lang and Titley (1998); Copper Creek: Lang and Titley (1998); Duoxiasongduo: Zengqian et al. (2003); El Abra: Cocker et al. (2015); El Salvador: Lee (2009); El Teniente: Cannell et al. (2005); Vry et al. (2010); Ertsberg: McMahon (1994); Frieda River: Mason and McDonald (1978); Whalen and Britten (1982); Fujiawu: Wang et al. (2005); Grasberg: McMahon (1994); Koloula: Chivas (1978); Los Pelambres: Reich et al. (2003); Malasongduo: Zengqian et al. (2003); Zengqian et al., 2003; Panguna: Ford(1976); Qulong: Yang et al., 2009; Hu et al., 2015; Ray and Christmas: Lang and Titley, (1998); Riduo: Zengqian et al. (2003); Safford: Lang and Titley (1998); Sanbujiala: Jian et al. (2015); Shuteen: Batkhishig et al. (2010); Sierrita: Anthony and Titley (1988); Skouries: Frei (1995); Tongchang: Wang et al. (2005); Tuwu-Yandong: Zhang et al. (2006); Waisoi: Imai (2007); Yandera: Watmuff (1978); Yulong: Jiang et al. (2008); Zengqian et al. (2003); Zhanaga: Zengqian et al. (2003).

Figure 3. Standard values for selected elements analysed using ICP-MS/ICP-ES (y-axis) and pXRF (x-axis). Equations for each regression line are shown in Table 2. A. Sr; B. MnO; and C. Y. Calibration curves (regression lines) for pressed-powder standard placed directly onto the pXRF detector were used to calibrate pXRF data collected on intact rocks slabs. Calibration curves for pressed-powder standards with a thin (4 µm) propylene film placed between the standard and the pXRF detection were used to calibrate loose pulp material prepared in press cups.

Figure 4. Rock slab from the Yerington district (YE16AA144) divided into 12 areas that were analysed by pXRF to assess instrument precision, sampling precision and the effect of epidote and albite alteration on Sr, Mn and Y values. Associated pXRF data are listed in Table 4.

Figure 5. Comparisons between pXRF data (mean values for a given sample) and conventional laboratory data for different sample media. A. Sr/Y: pXRF data from pulp material in press cups and ICP-MS/ICP-ES data. B. Sr/MnO: pXRF data from pulp material in press cups and ICP-MS/ICP-ES data. C. Sr/Y: pXRF data from intact rock slabs and ICP-MS/ICP-ES data. D. Sr/MnO: pXRF data from intact rocks slabs and ICP-MS/ICP-ES data. All data included in Tables 5 and 6.

Figure. 6. PXRF data of pre-, syn-, and post-mineralization intrusive rocks from six porphyry Cu and skarn districts plotted on Sr/MnO vs. Sr/Y diagrams using the fertility fields outlined in Figure 2. The sample medium analysed for each district is listed here. A. Yerington district, Nevada; rock slabs. For clarity, pulp powder analyses from Yerington are not included on this diagram. B. Resolution deposit, USA; rock slabs. C. Las Bambas district, Peru; rock slabs. D. Cadia district, Australia; pulp powders. E. Cowal district, Australia; pulp powders and rock slabs; and F. Northparkes district, Australia; pulp powders. 1σ error bars are shown for each datapoint and were calculated as one standard deviation from the mean of multiple analyses on each sample. Where error bars are not visible, they are smaller than the symbol size. Mean Sr/Y and Sr/MnO values for each

sample in each dataset are included in Tables 5 and 6. Data from individual analyses are tabulated in Appendix B.

Figure 7. Mean values of Sr/MnO and Sr/Y for each category of intrusion (pre-, syn-, and post-mineralization intrusive rocks) from the Yerington district. Light grey shaded symbols are individual datapoints, as shown in Figure 6A. Fertility fields are those outlined in Figures 2 and 6. 1σ error bars are shown for each mean value and were calculated as one standard deviation from the mean. Calculated mean and standard deviation values for the pre-, syn- and post-mineralization Yerington datasets are listed in Table 5. Data from individual analyses are tabulated in Appendix B.

Table captions

Table 1. Summary of the intrusive geological history from deposit locations used in this study showing pre-, syn-, and post-mineralisation intrusions in each district.

Table 2. Calibration factors and correlation coefficients applied to pXRF data.

Table 3. Analytical precision of Sr, Y and Mn measured by pXRF instruments compared to average values of samples analysed in this study. Standards and blanks were excluded from average value calculations due to the absence or low concentrations of some elements.

Table 4. Measurements of analytical and sampling precision for the Olympus Vanta pXRF. All element concentrations are in ppm. Spot locations are shown on Figure 4.

Table 5. ICP- and pXRF data for intact rock slabs. Relative standard deviation (RSD) values are shown for multiple analyses collected on individual samples. The relative differences (RD) between pXRF and ICP data are also shown.

Table 6. ICP- and pXRF data for pulp powders. Relative standard deviation (RSD) values are shown for multiple analyses collected on individual samples. The relative differences (RD) between pXRF and ICP data are also shown.

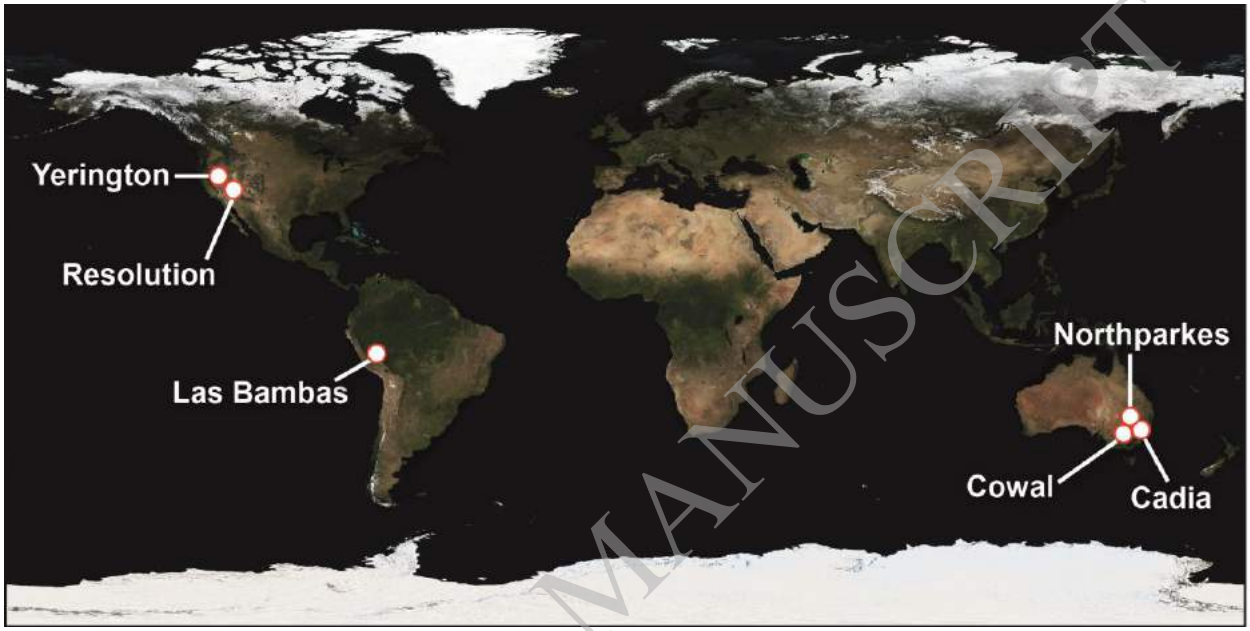

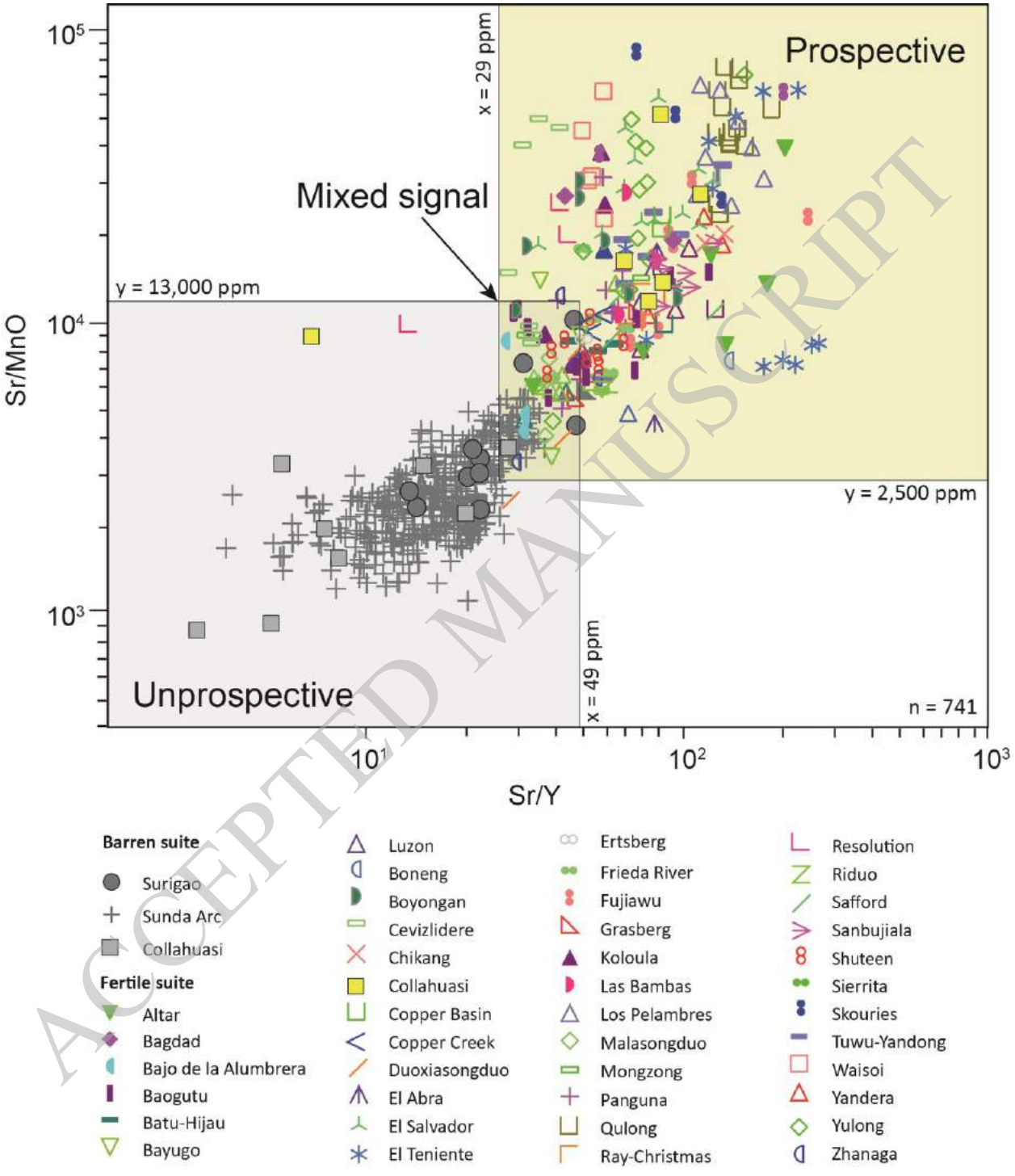

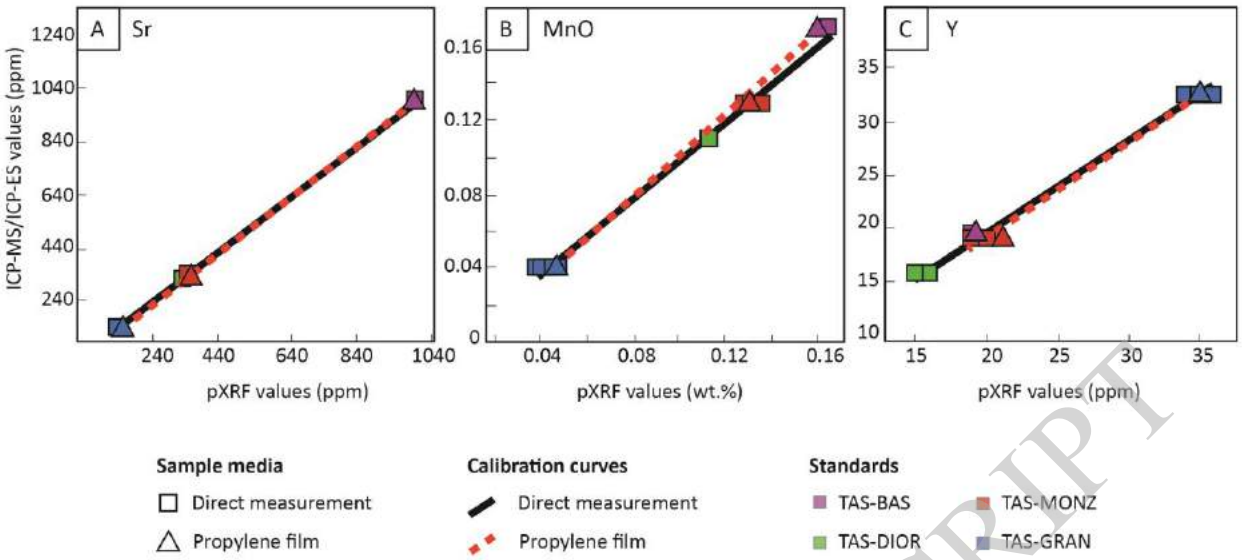

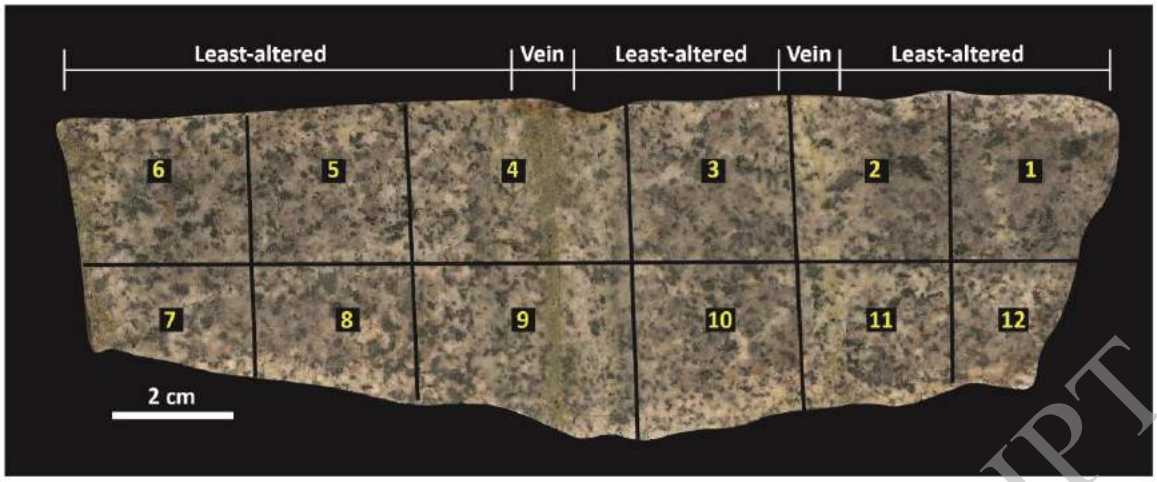

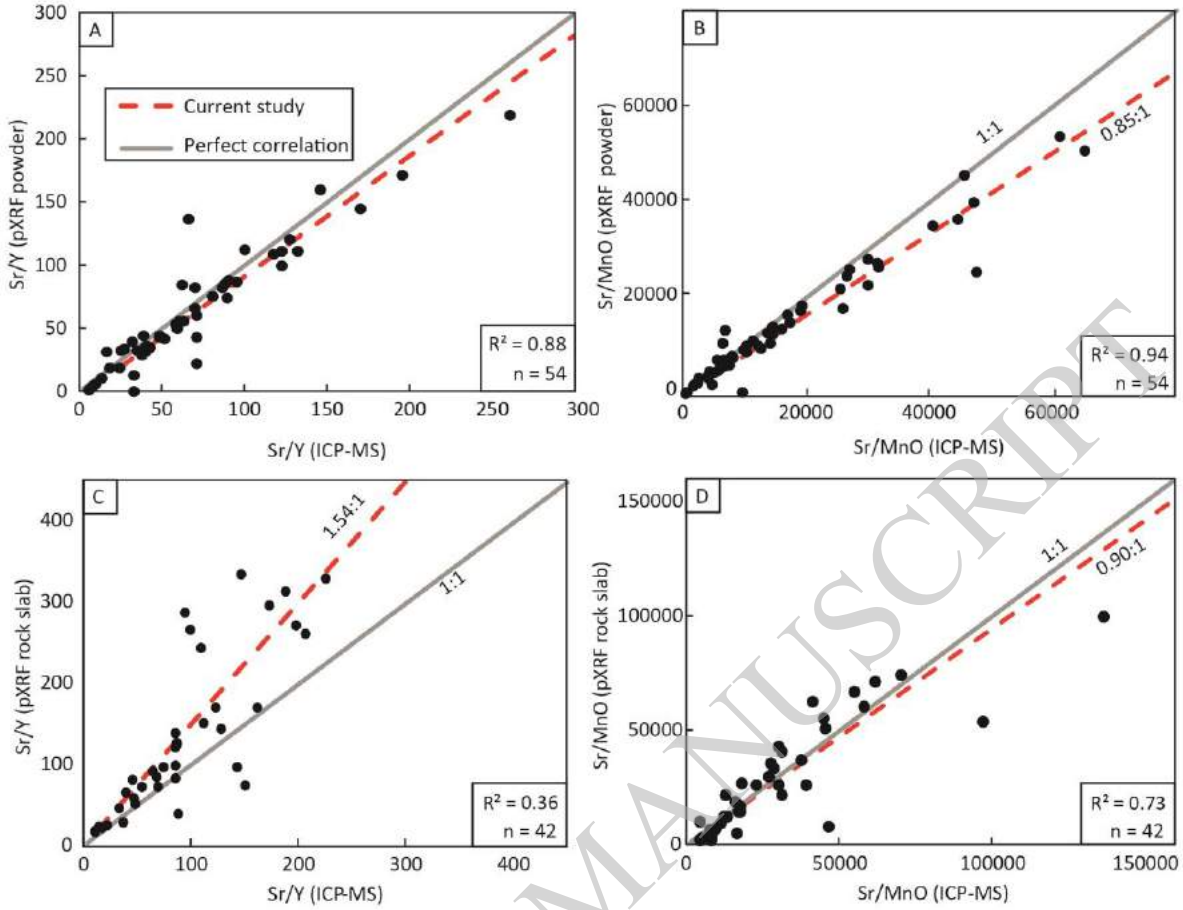

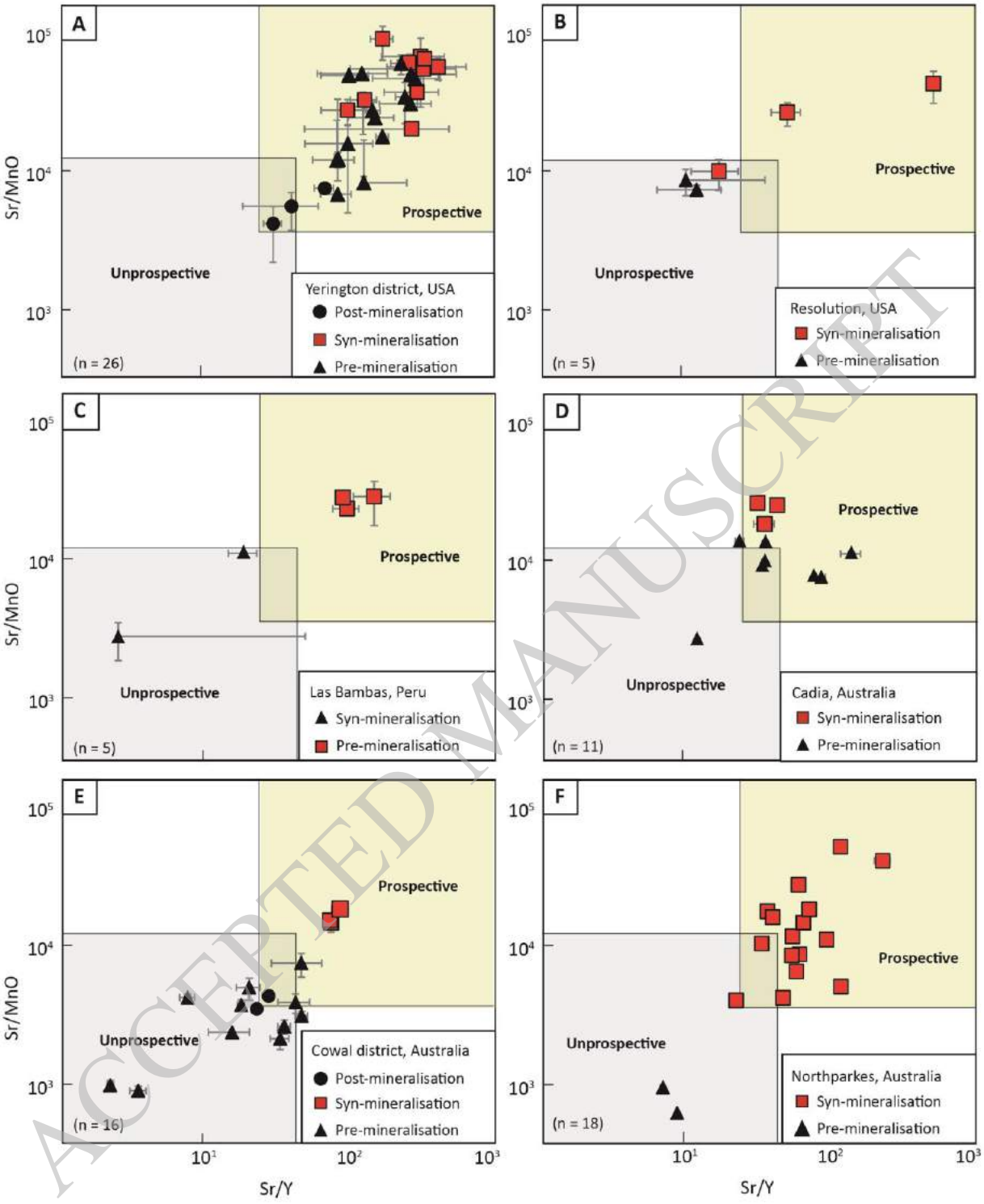

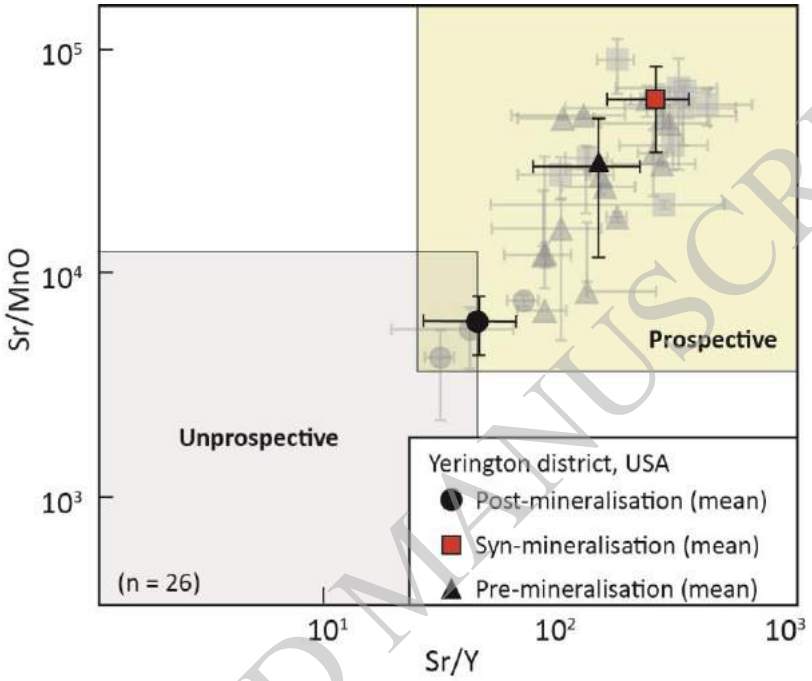

Table 1. Summary of the intrusive geological history from deposit locations used in this study showing pre-, syn-, and post-mineralisation intrusions in each district.

			Pre-mineralisation rocks		Syn-mineralisation rocks		Post-mineralisation rocks		
Geological site	**Deposit type**	**Country**	**Unit**	**Age (Ma)**	**Unit**	**Age (Ma)**	**Unit**	**Age (Ma)**	**Reference**
Yerington	Porphyry Cu-Mo (	USA	McLeod Hill monz	169.4 ± 0.4	Luhr Hill granite	168.5 ± 0.4	Shamrock monzor	165.8 ± 0.4	Dilles (1987); Dilles and Wright (1988) Banik et al. (2017)
			Bear monzonite						
Resolution	Porphyry Cu (±M	USA	Silver King quartz	74	Schultze granite	67 - 61	-	-	Creasy (1980)
Las Bambas	Skarn-Cu	USA	Pioneros diorite	38.1	Jauapaylla monzoc	33.8	-		Cannell et al. (2017)
			Rayusco diorite		Ferrobamba quartz	-			
					La Cresta quartz r	-			
Cowal	Porphyry-epithern	Australia	E43 diorite		Marsden granodior		Muddy Lake diorit		Zukowski (2010); Rush (2013)
			E43 quartz diorite		E43 quartz feldspar porphyry		E42 monzonite		
			E43 granodiorite		Lake monzonite				
			Marsden quartz di		Lake diorite				
			Marsden granodior						
			E41 monzonite						
			Dewars diorite						
Northparkes	Porphyry Cu-Au	Australia	-	-	Porphyry 1	444 – 439	Trachyte	-	Lickfold et al. (2003)
			-	-	Porphyry 2		Monzonite	-	
			-	-	Biotite quartz monzonite				
Cadia	Porphyry Au-Cu	Australia	Turnbridge Wells (	-	Cadia Far East mc	-	-	-	Wilson (2003)
			Cadia Hill monzor	-		-	-	-	
			Cadia Quarry mor	-		-	-	-	

Table 2. Calibration factors and correlation coefficients applied to pXRF data.

	Olympus Vanta	
Element	**Factor**	**R^2**
Direct measurement		
Sr	1.00	1.00
MnO	1.01	0.99
Y	0.97	0.98
Through propylene film		
Sr	1.02	1.00
MnO	1.11	1.00
Y	0.87	0.98

Table 3. Analytical precision of Sr, Y and Mn measured by pXRF instruments compared to average values of samples analysed in this study. Standards and blanks were excluded from average value calculations due to the absence or low concentrations of some elements.

	Olympus Vanta (n = 362)		
	Mean value* (ppm)	**Error (ppm)**	**Error (%)**
Sr	748	± 3.0	0.4
Y	12	± 1.4	11
Mn	710	± 12	1.7

* Calculated mean value of all pXRF data of intrusive rocks analysed in the current study

Table 4. Measurements of analytical and sampling precision for the Olympus Vanta pXRF. All element concentrations are in ppm. Spot locations are shown on Figure 4.

	Olympus Vanta pXRF										
Sample ID	**Spot**	**Mn**	**Sr**	**Y**	**Spot**	**Mn**	**Sr**	**Y**	**Spot**	**Mn**	**Sr**	**Y**
YE16AA144	4	396	803	6	5	499	1236	8	1	423	1252	9
YE16AA144	9	446	1613	8	5	501	1244	7	2	464	1151	9
YE16AA144	-	-	-	-	5	496	1239	8	3	478	1105	12
YE16AA144	-	-	-	-	5	503	1232	8	5	533	1157	13
YE16AA144	-	-	-	-	5	499	1240	8	6	525	1050	10
YE16AA144	-	-	-	-	5	509	1241	8	7	476	1149	10
YE16AA144	-	-	-	-	5	502	1234	8	8	548	1174	8
YE16AA144	-	-	-	-	5	508	1241	9	10	457	1178	9
YE16AA144	-	-	-	-	5	502	1250	8	11	583	1039	12
YE16AA144	-	-	-	-	5	510	1238	8	12	489	1170	10
Mean		*421*	*1208*	*7*		*503*	*1240*	*8*		*498*	*1143*	*10*
Standard deviation		*35*	*573*	*1.4*		*4.7*	*5.1*	*0.5*		*48.6*	*63.2*	*1.6*
Relative standard deviation		*8.4*	*47.4*	*20.2*		*0.9*	*0.4*	*5.9*		*9.8*	*5.5*	*15.9*

Table 5. ICP- and pXRF data for intact rock slabs. Relative standard deviation (RSD) values are shown for multiple analyses collected on individual samples. The relative differences (RD) between pXRF and ICP data are also shown.

				ICP-MS/ICP-ES		pXRF - rock slabs: Mean					pXRF- rock slabs: Standard deviation		pXRF - rock slab: RSD		RD (pXRF vs ICP-MS/ICP-ES)	
District	**Sample ID**	**Unit name/rock type**	**Relative timing**	**Sr/Y**	**Sr/MnO**	**MnO wt%**	**Sr ppm**	**Y ppm**	**Sr/MnO**	**Sr/Y**	**Sr/MnO**	**Sr/Y**	**Sr/MnO**	**Sr/Y**	**Sr/Y**	**Sr/MnO**
Cowal	CD17CL005	Lake diorite	Syn-mineralisation	69	15160	0.048	707.3	9.7	14971	73	2799	2	19	3	6	1
	CD17CL064	E43 diorite	Pre-mineralisation	34	2668	0.222	696.0	15.2	3152	46	349	4	11	10	35	18
	CD17CL069	E43 quartz diorite	Pre-mineralisation	13	3300	0.072	273.3	15.2	3781	18	456	1	12	6	39	15
	CD17CL111	E42 monzonite	Post-mineralisation	18	2719	0.187	593.3	27.7	3177	21	207	1	7	3	19	17
	CD17CL137	Dewars diorite	Post-mineralisation	24	2877	0.090	339.0	12.9	3772	26	308	2	8	7	10	31
	CL17CD001	Lake monzonite	Syn-mineralisation	55	16100	0.018	278.0	3.9	15520	72	1725	2	11	3	31	4
Las Bambas	LB15DC027	Ferrobamba monzodiorite	Syn-mineralisation	85	16740	0.040	999.7	7.8	27509	138	12602	38	46	27	63	64
	LB15DC035	Jahuapaylla monzodiorite	Syn-mineralisation	65	10986	0.044	965.9	10.9	22416	91	2947	18	13	20	40	104
	LB16AG048	La Cresta monzodiorite	Syn-mineralisation	68	28750	0.041	1114.9	13.1	27012	85	1102	5	4	6	25	6
	LB16AG009	Pioneros quartz diorite	Post-mineralisation	149	6342	0.072	216.8	2.7	2642	75	1061	45	40	60	50	58
	LB16AG162	Rayusco diorite	Post-mineralisation	16	2480	0.042	443.1	18.6	10615	24	369	4	3	16	51	328
Resolution	RE16JP022	Schultz granite	Syn-mineralisation	46	29000	0.016	609.7	4.4	43405	517	14760	728	34	141	1025	50
	RE15JP023	Schultz granite	Syn-mineralisation	49	21533	0.025	637.7	12.9	26886	51	6819	12	25	23	5	25
	RE15JP061	Schultz granite	Syn-mineralisation	13	9375	0.022	215.3	12.9	10086	17	3344	6	33	35	34	8
	RE16JP077	Quartz diorite	Pre-mineralisation	48	5927	0.098	721.7	12.3	7413	59	816	6	11	10	23	25
	RE16JP075	Quartz diorite	Pre-mineralisation	42	3700	0.097	803.0	10.3	8727	83	2486	26	28	31	97	136
Yerington	YE16AA082	Shamrock monzonite	Post-mineralisation	88	14702	0.103	585.0	17.1	6046	39	2426	21	40	54	56	59
	YE16AA097	Shamrock monzonite	Post-mineralisation	41	7689	0.077	628.3	9.7	8187	66	671	10	8	15	62	6
	YE16AA112	Shamrock monzonite	Post-mineralisation	38	6052	0.116	454.0	15.8	4526	29	2509	4	55	14	24	25
						Mean			6253	45						
						Standard deviation			1839	19						
	YE16AA237	McLeod Hill quartz monzodiorite	Pre-mineralisation	47	10403	0.047	617.0	8.1	13128	81	1223	26	9	32	72	26
	YE16AA200	McLeod Hill quartz monzodiorite	Pre-mineralisation	85	96880	0.020	1035.7	11.6	54461	98	16265	36	30	36	16	44
	YE16AA226	McLeod Hill quartz monzodiorite	Pre-mineralisation	109	36263	0.027	1007.3	4.2	37852	243	2306	35	6	14	123	4
	YE16AA012	Bear quartz monzonite	Pre-mineralisation	85	43770	0.014	769.0	8.1	55981	121	16516	62	30	51	42	28
	YE16AA013	Bear quartz monzonite	Pre-mineralisation	94	44330	0.020	1035.3	3.9	51634	285	11453	141	22	50	204	16
	YE16AA014	Bear quartz monzonite	Pre-mineralisation	87	45385	0.032	996.0	2.0	8961	125	8961	125	100	100	44	80
	YE16AA060	McLeod Hill quartz monzodiorite	Pre-mineralisation	47	7572	0.049	362.0	4.5	7384	82	839	20	11	24	74	2
	YE16AA066	McLeod Hill quartz monzodiorite	Pre-mineralisation	111	38030	0.039	1012.7	7.4	26692	150	6645	53	25	35	35	30
	YE16AA069	McLeod Hill quartz monzodiorite	Pre-mineralisation	127	25543	0.053	1406.0	9.9	30050	144	13045	19	43	13	13	18
	YE16AA131	McLeod Hill quartz monzodiorite	Pre-mineralisation	75	15748	0.080	1372.7	16.1	17270	96	1312	48	8	50	28	10
	YE16AA144	McLeod Hill quartz monzodiorite	Pre-mineralisation	122	14588	0.062	1191.3	7.1	19466	169	2296	17	12	10	38	33
	YE16AA169	McLeod Hill quartz monzodiorite	Pre-mineralisation	85	11424	0.096	1273.3	15.5	13322	82	1126	2	8	3	3	17
	YE16AA192	Bear quartz monzonite	Pre-mineralisation	99	27055	0.033	1097.7	4.5	33693	265	3293	105	10	40	168	25
						Mean			28453	149						
						Standard deviation			17288	72						
	YE16AA238	Luhr Hill granite	Syn-mineralisation	141	25807	0.021	607.0	6.8	30280	96	8653	33	29	35	32	17
	YE16AA215	Luhr Hill granite	Syn-mineralisation	160	137570	0.013	1282.3	7.7	100057	169	36273	31	36	18	6	27
	YE16AA044	Luhr Hill granite	Syn-mineralisation	87	26180	0.017	598.3	4.8	36029	127	6073	26	17	21	46	38
	YE16AA065	Luhr Hill granite	Syn-mineralisation	117	40313	0.020	1181.0	3.5	62695	416	15369	235	25	56	256	56
	YE16AA070	Luhr Hill granite	Syn-mineralisation	185	69480	0.023	1277.5	4.6	74547	313	48192	146	65	47	69	7
	YE16AA135	Luhr Hill granite	Syn-mineralisation	203	53915	0.014	909.0	3.5	67097	260	14584	45	22	18	28	24
	YE16AA157	Luhr Hill granite	Syn-mineralisation	170	30057	0.021	790.3	2.9	40974	295	11308	122	28	41	74	36
	YE16AA163	Luhr Hill granite	Syn-mineralisation	195	29953	0.022	485.7	2.6	22143	271	1295	223	6	82	39	26
	YE16AA166	Luhr Hill granite	Syn-mineralisation	221	57570	0.015	833.3	4.8	60638	327	23655	226	39	69	48	5
	YE16AA181	Luhr Hill granite	Syn-mineralisation	145	60820	0.018	1229.7	3.9	71541	333	13134	94	18	28	130	18
						Mean			56600	261			**Mean**	**24**	**32**	**Mean**	**78**	**37**
						Standard deviation			23909	101								

Table 6. ICP- and pXRF data for pulp powders. Relative standard deviation (RSD) values are shown for multiple analyses collected on individual samples. The relative differences (RD) between pXRF and ICP data are also shown.

				ICP-MS/ICP-ES		pXRF - pulp powders: Mean					pXRF - Pulp powders: Standard deviation		pXRF - Pulp powders: RSD			RD (pXRF vs ICP-MS/ICP-ES)	
District	**Sample ID**	**Unit name/rock type**	**Relative timing**	**Sr/Y**	**Sr/MnO**	**MnO**	**Sr**	**Y**	**Sr/MnO**	**Sr/Y**	**Sr/MnO**	**Sr/Y**	**Sr/MnO**	**Sr/Y**		**Sr/MnO**	**Sr/Y**
						wt.%	**ppm**	**ppm**					**%**	**%**		**%**	**%**
Cadia	151708	Diorite	Pre-mineralisation	61	5781	0.198	1483	17.3	7481	86	300	6	4	7		29	41
	151709	Diorite	Pre-mineralisation	65	6522	0.131	1451	10.7	11098	138	687	21	6	15		70	112
	151790	Monzonite	Syn-mineralisation	25	25950	0.034	627	17.6	18251	36	430	6	2	16		30	45
	152862	Monzonite	Syn-mineralisation	50	26567	0.036	912	20.7	25032	44	684	2	3	4		6	12
	152863	Monzonite	Syn-mineralisation	36	47300	0.020	507	15.5	25875	33	1335	1	5	3		45	9
	152865	Monzonite	Pre-mineralisation	41	10071	0.080	773	21.2	9619	36	9	1	0	3		4	11
	152866	Monzonite	Pre-mineralisation	38	13760	0.057	740	20.2	13086	37	340	1	3	4		5	4
	152867	Monzonite	Pre-mineralisation	39	10317	0.073	671	18.8	9161	36	114	0	1	0		11	9
	152868	Diorite	Pre-mineralisation	79	7375	0.167	1244	16.0	7467	78	26	0	0	0		1	2
	152869	Diorite	Pre-mineralisation	12	2510	0.200	534	41.4	2667	13	51	0	2	0		6	7
	152871	Diorite	Pre-mineralisation	70	7013	0.106	842	14.8	13670	25	261	2	2	6		95	65
Cowal	168147	E41 diorite	Pre-mineralisation	23	2260	0.215	564	16.0	2645	35	414	3	16	10		17	53
	168163	E41 diorite	Pre-mineralisation	15	1844	0.225	474	14.4	2149	33	450	5	21	14		17	120
	168172	E41 diorite	Pre-mineralisation	30	2798	0.175	681	16.6	3946	42	843	10	21	24		41	40
	168630	E41 monzonite	Pre-mineralisation	31	9703	0.048	46	19.8	989	2	110	0	11	5		90	92
	168674	E41 monzonite	Pre-mineralisation	31	4781	0.126	301	20.4	2401	16	4	5	0	31		50	50
	177113	Marsden quartz diorite	Pre-mineralisation	4	898	0.103	92	25.4	901	4	99	0	11	12		0	9
	177118	Marsden quartz diorite	Pre-mineralisation	17	4396	0.078	388	19.1	5069	20	1216	4	24	18		15	20
	177126	Marsden quartz diorite	Pre-mineralisation	37	6871	0.093	691	16.3	7604	46	1969	17	26	37		11	24
	177127	Marsden quartz monzodiorite	Pre-mineralisation	8	4288	0.029	122	15.7	4291	8	327	1	8	12		0	2
	177134	Marsden granodiorite	Syn-mineralisation	69	19303	0.032	607	7.3	18837	84	1834	11	10	13		2	22
Yerington	YE16AA013	Bear quartz monzonite	Pre-mineralisation	94	44330	0.025	924	10.4	36766	89	0	0	0	0		17	5
	YE16AA014	Bear quartz monzonite	Pre-mineralisation	87	45385	0.021	947	10.8	46021	88	2312	5	5	6		1	1
	YE16AA065	Luhr Hill granite	Syn-mineralisation	117	40313	0.034	1190	10.8	35430	110	42	8	0	7		12	6
	YE16AA069	McLeod Hill quartz monzodiorite	Pre-mineralisation	127	25543	0.065	1439	11.8	22302	122	748	7	3	5		13	4
	YE16AA082	Shamrock monzonite	Post-mineralisation	88	14702	0.098	1257	16.5	12810	76	415	3	3	4		13	13
	YE16AA088	Shamrock monzonite	Post-mineralisation	47	31357	0.032	875	19.3	27643	45	838	1	3	3		12	4
	YE16AA097	Shamrock monzonite	Post-mineralisation	41	7689	0.097	635	17.0	6580	37	22	0	0	0		14	9
	YE16AA112	Shamrock monzonite	Post-mineralisation	38	6052	0.122	674	19.8	5505	34	84	0	2	0		9	10
	YE16AA144	McLeod Hill quartz monzodiorite	Pre-mineralisation	122	14588	0.082	1182	11.6	14464	102	321	5	2	5		1	16
	YE16AA157	Luhr Hill granite	Syn-mineralisation	170	30057	0.031	892	6.1	28605	146	787	15	3	10		5	14
	YE16AA163	Luhr Hill granite	Syn-mineralisation	195	29953	0.039	885	5.2	22988	172	618	22	3	13		23	12
	YE16AA169	McLeod Hill quartz monzodiorite	Pre-mineralisation	85	11424	0.106	1228	14.6	11582	84	236	4	2	5		1	1
	YE16AA181	Luhr Hill granite	Syn-mineralisation	145	60820	0.023	1216	7.5	53816	161	1791	0	3	0		12	11
	YE16AA192	Bear quartz monzonite	Pre-mineralisation	99	27055	0.041	1072	9.4	26332	114	0	0	0	0		3	15
	YE17AA237	McLeod Hill quartz monzodiorite	Pre-mineralisation	47	10403	0.064	677	14.6	10513	46	60	3	1	6		1	1
Northpark	NP17TW001	BQM	Syn-mineralisation	62	8000	0.154	1275	22.0	8255	58	43	3	1	5		3	6
	NP17TW007	BQM	Syn-mineralisation	57	6767	0.141	872	15.7	6190	55	84	2	1	4		9	3
	NP17TW016	BQM	Syn-mineralisation	89	12318	0.051	573	11.0	10606	90	219	7	2	7		14	1
	NP17TW017	Porphyry 2	Syn-mineralisation	58	14175	0.051	573	11.0	11156	52	47	2	0	5		21	10
	NP17TW022	Porphyry 1	Syn-mineralisation	70	4200	0.043	169	3.8	3969	45	113	1	3	1		5	36
	NP17TW023	BQM	Syn-mineralisation	59	31633	0.034	918	16.0	26758	57	1683	0	6	0		15	3
	NP17TW025	Porphyry 2	Syn-mineralisation	122	64750	0.025	1270	11.3	51007	112	2055	1	4	1		21	8
	NP17TW026	Porphyry 2	Syn-mineralisation	261	46950	0.022	889	4.1	40183	220	2045	27	5	12		14	16
	NP17TW028	Porphyry 2	Syn-mineralisation	70	16075	0.043	611	9.9	14105	62	170	4	1	7		12	12
	NP17TW030	Porphyry 1	Syn-mineralisation	36	12800	0.026	262	8.2	9897	32	236	2	2	6		23	12
	NP17TW032	Porphyry 2	Syn-mineralisation	33	17000	0.019	327	9.4	17048	35	669	3	4	10		0	6
	NP17TW037	BQM	Syn-mineralisation	39	17475	0.043	669	17.7	15475	38	502	2	3	5		11	3
	NP17TW046	Porphyry 1	Syn-mineralisation	69	19200	0.033	576	8.5	17644	68	262	0	1	0		8	1
	NP17TW050	BQM	Syn-mineralisation	22	4245	0.121	459	21.7	3793	21	106	1	3	4		11	4
	NP17TW058	Porphyry 1	Syn-mineralisation	132	5077	0.134	640	5.7	4782	113	37	0	1	0		6	14
	Np17TW047	Porphyry 1	Syn-mineralisation	58	8280	0.052	419	8.2	8109	52	297	3	4	7		2	11
	NP17TW087	Trachyte	Pre-mineralisation	6	925	0.262	229	34.8	874	7	16	0	2	3		6	9
	NP17TW088	Monzonite	Pre-mineralisation	8	592	0.279	158	19.1	566	8	4	0	1	3		4	3
													Mean	**5**	**7**	**Mean**	**16**	**19**